

PAPER • OPEN ACCESS

From local to nonlocal: higher fidelity simulations of photon emission in intense laser pulses

To cite this article: T G Blackburn *et al* 2021 *New J. Phys.* **23** 085008

View the [article online](#) for updates and enhancements.

You may also like

- [Modulation of Weyl semimetal state in half-Heusler GdPtBi enabled by hydrostatic pressure](#)
Junli Zhang, Lei Jin, Jie Chen *et al.*
- [Positive mass theorems for asymptotically hyperbolic Riemannian manifolds with boundary](#)
Piotr T Chrusciel and Gregory J Galloway
- [Collective self-trapping of atoms in a cavity](#)
A Dombi, T W Clark, F I B Williams *et al.*



PAPER

From local to nonlocal: higher fidelity simulations of photon emission in intense laser pulses

OPEN ACCESS

RECEIVED
24 March 2021REVISED
4 August 2021ACCEPTED FOR PUBLICATION
9 August 2021PUBLISHED
27 August 2021Original content from
this work may be used
under the terms of the
[Creative Commons
Attribution 4.0 licence](#).Any further distribution
of this work must
maintain attribution to
the author(s) and the
title of the work, journal
citation and DOI.T G Blackburn^{1,*} , A J MacLeod² and B. King² ¹ Department of Physics, University of Gothenburg, SE-41296 Gothenburg, Sweden² Centre for Mathematical Sciences, University of Plymouth, Plymouth, PL4 8AA, United Kingdom

* Author to whom any correspondence should be addressed.

E-mail: tom.blackburn@physics.gu.se**Keywords:** Compton scattering, strong-field QED, radiation reactionSupplementary material for this article is available [online](#)**Abstract**

State-of-the-art numerical simulations of quantum electrodynamical (QED) processes in strong laser fields rely on a semiclassical combination of classical equations of motion and QED rates, which are calculated in the locally constant field approximation. However, the latter approximation is unreliable if the amplitude of the fields, a_0 , is comparable to unity. Furthermore, it cannot, by definition, capture interference effects that give rise to harmonic structure. Here we present an alternative numerical approach, which resolves these two issues by combining cycle-averaged equations of motion and QED rates calculated in the locally monochromatic approximation. We demonstrate that it significantly improves the accuracy of simulations of photon emission across the full range of photon energies and laser intensities, in plane-wave, chirped and focused background fields.

1. Introduction

The collision of multi-GeV electron beams and intense laser pulses is a promising scenario for precision measurements of quantum electrodynamics (QED) in the strong-field regime, where both the normalised amplitude of the laser, a_0 , and quantum nonlinearity parameter of the electron, χ_e , exceed unity. Perturbative QED calculations of the interaction fail once $a_0 \ll 1$ and must be replaced by ‘all-order’ approaches, which take the interaction with the strong background field into account exactly [1, 2]. While the theory for this regime is now several decades old [3], experiments are limited in number. In the weakly multiphoton regime, $a_0 \simeq 0.4$, laser-electron collision experiments have observed Compton scattering (photon emission) and trident electron–positron pair creation [4, 5]. At higher values of a_0 , but small χ_e , they have observed photon emission in the classical regime (nonlinear Thomson scattering) [6–9] and at $a_0 \simeq 10$, radiation reaction (multiple photon emission) in the nonlinear classical [10] and quantum regimes [11]. However, as yet, there are no experimental measurements charting the transition between the perturbative, multiphoton, and nonlinear regimes, $0.1 \lesssim a_0 \lesssim 10$ at $\chi_e \simeq 1$. This is likely to change in the near future, as increasing interest in strong-field QED has led to planned experiments that will combine conventional electron accelerators with intense optical lasers [12, 13].

The transition regime represents a particular challenge for theory and simulation. A perturbative approach is not sufficient once $a_0 \ll 1$. However, neither is an approach based on the *locally constant field approximation* (LCFA) [1, 14], as this applies only in the opposite limit, $a_0 \gg 1$: this approximation underpins the simulation codes [15–17] used to model QED effects in laser–plasma interactions [18–24], which will be explored in the next generation of multi-petawatt laser facilities [25–28]. The versatility of the LCFA comes from its local nature and the neglect of interference effects, i.e. the finite size of the spacetime region over which QED processes take place, which requires both $a_0 \gg 1$ and $a_0^3/\chi_e \gg 1$; the limitations of doing so have been thoroughly discussed in the literature [29–33]. Experiments that aim at precision

measurements of strong-field QED demand precision simulations of the interaction. However, in the transition regime, the error made by simulations based on LCFA rates is unacceptably large.

In this paper, we present a simulation framework that overcomes these issues by using the *locally monochromatic approximation* (LMA) instead. This achieves greater accuracy by taking into account interference effects at the scale of the laser wavelength, which is possible provided that the laser pulse is relatively unchanged by the collision with a probe electron beam. To do this, we combine classical trajectories, defined on a cycle-averaged basis, with probability rates that treat the background ‘locally’ as a monochromatic plane wave, with an amplitude and frequency that can vary in space and time. As such, we exchange the ability of the LCFA to model an *arbitrary* electromagnetic field for significantly increased accuracy in the modeling of *plane-wave-like* fields. While plane-wave rates have already been used in numerical modeling and analysis [13, 34–36], their derivation from strong-field QED has only recently been formalised by Heinzl *et al* [37], who combine a slowly varying envelope approximation [38–41] with a ‘local’ expansion in the interference phase [1, 3, 29, 31, 32, 42].

The derivation of the LMA in Heinzl *et al* [37] assumes a plane wave, whereas any experimental configuration will employ a focused laser pulse. This makes it essential to consider beyond-plane-wave field configurations, for which exact theoretical results are limited in number [43, 44]. In order to make progress, we consider the case of plane-wave backgrounds that have a nonlinear dependence on phase, or a ‘chirp’, which results in a localisation of both the wave’s amplitude and frequency. By allowing both the amplitude and wavevector to vary in space and time, we gain analytical insight into the case of a focused background, where this would also be the case. We then describe how the LMA may be implemented in numerical simulations of photon emission and benchmark their predictions against strong-field QED for pulsed plane waves (unchirped and chirped) as well as with focusing pulses. For the last of these, we must employ an approximate solution to the Dirac equation [45–47], which, to the best of our knowledge, has not previously been compared to a simulation. Our results confirm that simulations based on this framework may be used for precision modeling of experiments, with an accuracy of a few percent in the integrated probability (improving on the accuracy of the LCFA by orders of magnitude in the transition regime), and correct reproduction of harmonic structure in the differential spectrum, which has been identified as an aim of future experiments [13].

In the following, we use a system of units in which the Planck’s reduced constant, the speed of light and the vacuum permittivity are all set to unity: $\hbar = c = \epsilon_0 = 1$. The electron mass is denoted by m . The fine-structure constant α is related to the elementary charge e by $\alpha = e^2/(4\pi)$.

2. Theory background

We begin with an explanation of how the full QED plane-wave results are calculated, as well as a summary of the main details arising from the analytical calculation underpinning the LMA. (Many papers have investigated the effect of pulse shape on nonlinear Compton scattering, see e.g. [40, 48–52].) For concreteness, we specify from the outset that we will be assuming a background that is a circularly polarised, chirped, plane-wave pulse with potential A . We define the dimensionless potential $a = eA/m$,

$$a(\phi) = a_0 f\left(\frac{\phi}{\Phi}\right) [\varepsilon \cos b(\phi) + \beta \sin b(\phi)], \quad (1)$$

where a_0 is the dimensionless intensity parameter [53] (also called the ‘classical nonlinearity’, normalised amplitude or the strength parameter) and ε, β are orthonormal polarisation vectors obeying $\varepsilon \cdot \varepsilon = \beta \cdot \beta = -1$. Throughout, we use lightfront coordinates $x^\mu = (x^+, x^-, \vec{x}^\perp)^\mu$, where $x^\pm = x^0 \pm x^3$, $\vec{x}^\perp = (x^1, x^2)$, $x^\pm = 2x_\mp$ and $\vec{x}^\perp = -\vec{x}_\perp$. The function $f(\phi/\Phi)$ is the pulse envelope which depends on the lightfront phase $\phi = \kappa \cdot x$ (where $\kappa_\mu = \delta_\mu^+ \kappa_+$ is the background wavevector), and the pulse phase duration, Φ , is related to the number of cycles, N , via $\Phi = 2N$. The function $b(\phi)$ describes the chirp of the background. For a pulse without chirp, b is linear in ϕ , i.e. $b''(\phi) = 0$ for all ϕ . (In the following, we will pick $b(\phi) = \phi$ for the unchirped case.)

We use the scattering matrix approach [54] to calculate the probability of single nonlinear Compton scattering from a single incoming electron colliding with a plane-wave background. We can write the scattering matrix element as:

$$\mathbf{S}_{r',r;l} = -ie \int d^4x \bar{\Psi}_{p',r'}(x) \not{\epsilon}_{k,l}^* e^{ik \cdot x} \Psi_{p,r}(x), \quad (2)$$

where $\hat{\epsilon}_{k,l}^*$ is the polarisation of the emitted photon with four-momentum k and $\Psi_{p,r}(\bar{\Psi}_{p',r'})$ is the Volkov wavefunction [55] of the incoming (outgoing) electron:

$$\Psi_{p,r}(x) = \left(1 + \frac{m \hat{\kappa} \cdot \hat{a}}{2 \kappa \cdot p}\right) u_{p,r} e^{iS_p(x)}, \quad S_p(x) = p \cdot x + \int^\phi dy \frac{2mp \cdot a(y) - m^2 a^2(y)}{2\kappa \cdot p}. \quad (3)$$

The matrix element can be simplified to:

$$S_{r',r;l} = \tilde{C} \int_{\phi_i}^{\phi_f} d\phi \bar{u}_{r'} \left[\Delta \hat{\epsilon}_{k,l}^* + \frac{m}{2 \kappa \cdot p} \left(\frac{\hat{a} \hat{\kappa} \hat{\epsilon}_{k,l}^*}{1-s} + \hat{\epsilon}_{k,l}^* \hat{a} \hat{\kappa} \right) \right] u_r \exp \left[\frac{i}{\eta_0(1-s)} \int_{\phi_i}^{\phi_f} dy \frac{k \cdot \pi(y)}{m^2} \right] \quad (4)$$

where $s = \kappa \cdot k / \kappa \cdot p$ is the lightfront momentum fraction of the emitted photon, $\eta_0 = \kappa \cdot p / m^2$ is the initial energy parameter of the probe electron, \tilde{C} contains normalisation constants, the instantaneous electron momentum is given by

$$\pi(y) = p - ma(y) + \kappa \frac{2m p \cdot a(y) - m^2 a^2(y)}{2 \kappa \cdot p}, \quad (5)$$

and the regularising factor $\Delta = 1 - k \cdot \pi / k \cdot p$ incorporates all the contributions from phases outside of the integral. The total probability can be written:

$$\mathbf{P} = \frac{\alpha}{\eta_0} \frac{1}{2^4 \pi^2} \int d^2 \vec{r}^\perp ds \frac{s}{1-s} \langle |\mathbf{S}_{r',r;l}|^2 \rangle_{\text{pol.}}, \quad (6)$$

where $\vec{r}^\perp = \vec{k}^\perp / (ms) - \vec{p}^\perp / m$ contains the shifted perpendicular momentum. Here $\langle \cdot \rangle^{\perp}$ indicates directions perpendicular to the background propagation direction and $\langle \cdot \rangle_{\text{pol.}}$ indicates an average over initial and sum over final polarisation states. The numerical results in exact QED are calculated by evaluating equation (6) directly: the matrix element in equation (2) was evaluated using photon polarisation eigenstates of the background [56] and spin states in the Lepage–Brodsky convention [57].

Rather than direct numerical evaluation, some of the integrals in equation (6) can be evaluated analytically by generalising the LMA [37] to arbitrarily chirped plane-wave pulses. In the following, we present an overview of this approach, and direct the reader to appendix A for details.

The background field is given by equation (1). For the LMA to approximate the emission spectrum well, the envelope function $f(\phi/\Phi)$ should be *slowly varying* with respect to the carrier frequency, implying that $\Phi^{-1} \ll \min[b'(\phi)]$ (i.e. $\Phi \gg 1$ for the unchirped case, which corresponds to a many-cycle pulse). However, in this work, we also include the chirp. Therefore we will also make a ‘slowly varying chirp’ approximation (see e.g. Seipt *et al* [58]). These approximations then allow the squared Kibble mass, μ , which occurs in an exponent, to be integrated over. The Kibble mass takes the form $\mu = 1 + \langle \vec{a}^2 \rangle_\theta - \langle \vec{a} \rangle_\theta^2$, where $\langle f \rangle_\theta = \theta^{-1} \int_{\phi-\theta/2}^{\phi+\theta/2} f$ denotes a phase-window average. In the case of a circularly polarised background, the slowly varying (envelope) and rapid (carrier) timescales occur in $\langle \vec{a} \rangle_\theta$. We can demonstrate the approximation by considering a single component of \vec{a} , e.g. $\vec{\epsilon} \cdot \vec{a}$.

$$\langle \vec{\epsilon} \cdot \vec{a} \rangle_\theta = \frac{a_0}{\theta} \int_{\phi-\theta/2}^{\phi+\theta/2} d\phi f\left(\frac{\phi}{\Phi}\right) \cos b(\phi). \quad (7)$$

Now, one can introduce a *local frequency scale*, $\omega(\varphi) = b'(\varphi)$ and integrate by parts as in equation (A6). The fast timescale of the cosine term is included *exactly*. The remaining terms for the envelope and chirp variations have a size, relative to the leading term, of the order of

$$\sim \frac{1}{\Phi} \frac{f'(\phi/\Phi)}{f(\phi/\Phi)}, \quad \sim \frac{\omega'(\phi)}{\omega(\phi)}, \quad (8)$$

respectively (neglecting a rapidly varying term that appears $\sim \cot b(\phi)$). As long as the magnitudes of both of these are much less than unity, we should expect the slowly varying approximation to be good. (The same arguments apply to the $\vec{\beta} \cdot \vec{a}$ term, whereas $\langle \vec{a}^2 \rangle_\theta$ is not affected by chirp in a circularly polarised background.) Beyond the additional constraints on the chirp, no further modifications to [37] are required in the derivation (more details are given in appendix A).

Finally, we arrive at $P^{\text{LMA}} = \int d\tau W^{\text{LMA}}$, where:

$$W^{\text{LMA}} = \sum_{n=1}^{\infty} \int_0^{s_{n,*}(\tau)} ds \frac{d^2 P_n^{\text{mono}} [a_{\text{rms}}(\tau), \eta(\tau)]}{d\tau ds}, \quad (9)$$

where $a_{\text{rms}}^2(\tau) = q^2/m^2 - 1$ and $\eta(\tau) = \omega[\phi(\tau)]\eta_0$, with $\eta_0 = \kappa \cdot p/m^2$ the *unchirped* energy parameter. Here $q = \langle \pi \rangle$ is the *quasimomentum*, the laser-cycle-average of the instantaneous electron momentum given in equation (5). The appearance of a *local* wavevector in $\eta(\tau)$ also follows from considering components of the field-strength tensor, $F^{\mu\nu}$, for the chirped pulse in equation (1), which contain terms $\sim \kappa^\mu(\phi)\partial a^\nu/\partial b$, where $\kappa^\mu(\phi) = b'(\phi)\kappa^\mu$. $\mathbf{P}_n^{\text{mono}}$ is the probability of nonlinear Compton scattering into the n th harmonic in a monochromatic background, τ is the proper time, related to the phase by $d\tau/d\phi = 1/(m\eta_0)$. The approximation is *locally* monochromatic because the intensity and energy parameter occurring in the monochromatic probability now take the (cycle-averaged) *local* value at the position of the electron. The integrand is given explicitly by equation (A28) for nonlinear Compton scattering. Unlike the monochromatic case, here the harmonic range is phase-dependent:

$$s_{n,*}(\tau) = \frac{s_n(\tau)}{1 + s_n(\tau)}, \quad s_n(\tau) = \frac{2m\eta(\tau)}{1 + a_{\text{rms}}^2(\tau)}, \quad (10)$$

where $s_n(\tau)$ is the edge of the classical (nonlinear) harmonic range.

To obtain the probability of Compton scattering in a focused laser background, we must use some approximation, as analytical solutions to the Dirac equation in a realistic focused laser background are unavailable (some progress has recently been made in this direction: see e.g. [43, 44]). One method is to find an approximate solution to the Dirac equation using a WKB expansion in a small parameter γ^{-1} , where γ is the initial relativistic gamma factor of the incident electron [45–47]. Then assuming $\gamma \gg a_0$, for a head-on collision of the electron probe with the focused laser pulse, one can write:

$$P^{2D} = \int d^2\vec{x}^\perp \rho(\vec{x}^\perp) P[a_{\text{rms}}(\vec{x}^\perp), \eta(\vec{x}^\perp)], \quad (11)$$

where ρ is the electron probe areal density and the plane-wave probability, \mathbf{P} from equation (6), now has an intensity parameter which can depend on the perpendicular spatial co-ordinate.

3. Implementation in numerical simulations

The inclusion of strong-field QED processes in numerical simulations, such as the particle-in-cell [15, 16] or particle-tracking codes [34, 35, 59] used in plasma and beam physics, is based on a semiclassical treatment of particle dynamics, which combines classical trajectories with the use of probability rates [60]. This is motivated by the appearance of the *classical* kinetic momentum π , equation (5), in the QED scattering probability, via the exponent of the Volkov wavefunction, equation (3). (This occurs because the Volkov solution is identical to the semiclassical solution of the Dirac equation in a plane-wave background.) This permits the probability, equation (6), to be approximated as the integral $\mathbf{P} \simeq \int W d\tau$, where $W \geq 0$ is interpreted as a probability rate, which can depend, inter alia, on the instantaneous momentum and field amplitude.

The approximations applied to the probability rate affect what dynamical quantities must be obtained from the classical trajectory. In the LCFA, for example, the rate $W = W[\chi(\tau)]$, where the quantum nonlinearity parameter $\chi(\tau) = e|F_{\mu\nu}[x(\tau)]\pi^\nu(\tau)|/m^3$ [1]. Furthermore, the conservation of momentum for the scattering may be written such that it constrains the kinetic, rather than asymptotic, momenta. Thus the classical trajectory must be defined in terms of kinetic momentum π , i.e. instantaneously, and obtained from the Lorentz force equation $d\pi_\mu/d\tau = -eF_{\mu\nu}\pi^\nu/m$ and $dx^\mu/d\tau = \pi^\mu/m$. This is illustrated on the left-hand side of figure 1: the classical trajectory is well-defined at all timescales, including that of the laser carrier wave. The angular structure of the photon emission arises from two sources: the oscillation of the trajectory ($\theta \simeq a_0/\gamma$ for $\gamma \gg a_0 \gg 1$) and the intrinsic beaming of the emission around the instantaneous velocity, the latter being of characteristic size $\theta \sim 1/\gamma$ [61, 62]. The former is the dominant contributor in the regime $a_0 \gg 1$, which is consequently where the LCFA is expected to be valid.

The rate in the LMA, by contrast, is derived assuming that the envelope of the potential, rather than the potential itself, is slowly varying. Averaging over the fast timescale, the laser period, means that the quantity that enters the rate, and also the conservation of momentum, is not the kinetic momentum directly, but rather the *quasimomentum* $q \equiv \langle \pi \rangle$ [1, 63]. In a plane wave, $\pi = p - ma + \kappa(2mp \cdot a - m^2 a^2)/(2\kappa \cdot p)$ and $\pi^2 = m^2$, whereas $q = p + \kappa m^2 a_{\text{rms}}^2/(2\kappa \cdot p)$ and $q^2 = m^2(1 + a_{\text{rms}}^2)$, for $a_{\text{rms}}^2 \equiv -\langle a^2 \rangle$. In contrast to the LCFA case, the rate is a function of two parameters: the normalised amplitude (or intensity parameter), a_{rms} , and the energy parameter $\eta \equiv \kappa \cdot p/m^2$, both locally defined. (The root-mean-square quantum parameter follows as $\chi_{\text{rms}} = a_{\text{rms}}\eta$.) Both may be obtained from q as follows: $a_{\text{rms}} = \sqrt{(q/m)^2 - 1}$ and $\eta = \kappa \cdot q/m^2$. An equation of motion for the quasimomentum may be obtained by separating the Lorentz force equation (in a focused, pulsed electromagnetic wave) into quickly and slowly varying components and

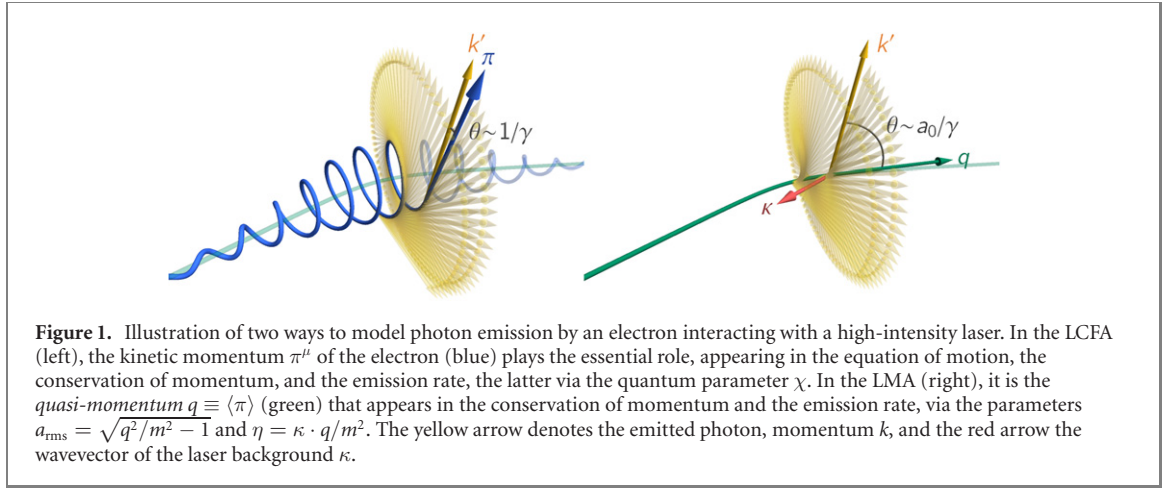


Table 1. Overview of the conceptual differences between LCFA- and LMA-based simulations of photon emission in strong laser pulses.

	LCFA	LMA
Rate derived for	Constant, crossed field	Monochromatic plane wave (fast quiver motion here)
and controlled by	Instantaneous momentum π^μ via quantum parameter χ_e	Quasimomentum $q^\mu = \langle \pi^\mu \rangle$ via a_{rms} and η
equation of motion	Lorentz force: $\frac{d\pi_\mu}{d\tau} = -\frac{eF_{\mu\nu}\pi^\nu}{m}$ (fast quiver motion here)	Ponderomotive force: $\frac{d\vec{q}}{dt} = -\frac{m^2}{2q^0} \frac{\partial a_{\text{rms}}^2}{\partial \vec{r}}$

isolating the latter. The result is the relativistic ponderomotive force equation [64]:

$$\frac{d\vec{q}}{dt} = -\frac{m^2}{2q^0} \frac{\partial a_{\text{rms}}^2}{\partial \vec{r}}, \quad (12)$$

where $q^0 = [m^2(1 + a_{\text{rms}}^2) + |\vec{q}|^2]^{1/2}$. The slowly varying components of the position are determined by

$$\frac{d\vec{r}}{dt} = \frac{\vec{q}}{q^0}. \quad (13)$$

The trajectory obtained from these two equations does not include the fast oscillation at the timescale of the laser period, as shown on the right-hand side of figure 1. This does not mean that the physical effect of that oscillation is lost: it is accounted for in the emission rate. To see this more clearly, note that at fixed s , in the limit $a_0 \gg 1$, there is a most probable harmonic index $n = a_{\text{rms}}^2 s / [\eta(1 - s)]$ [65]. Combining this relation with the conservation of quasimomentum, which reads $k_\perp^2/m^2 = 2n\eta s(1 - s) - s^2(1 + a_{\text{rms}}^2)$ for $p_\perp = 0$, one finds that the most probable emission angle is $\theta \simeq a_{\text{rms}}/\gamma$ for $\gamma \gg a_0 \gg 1$ [65] (see also [63]). Thus an equivalent angular structure emerges, provided that the classical trajectory is parametrised in terms of quasimomentum. The conceptual differences between LCFA- and LMA-based simulations are summarized in table 1.

The emission of photons, and its effect on this trajectory, is modeled in the following way. At any particular timestep, we have the electron quasimomentum q and position r from the classical equations of motion, as well as the local values of the laser normalised amplitude $a_{\text{rms}}(r)$, wavevector $\kappa(r)$ and polarisation (taken to be circular throughout). In fact, κ and q are sufficient to determine the properties of the emission, as they define the two invariant parameters, a_{rms} and η , that control the rate and the conservation of momentum. This is given by

$$q + n\kappa = q' + k, \quad (14)$$

where q' is the electron quasimomentum after the scattering, k is the momentum of the emitted photon, and n is the harmonic index (the net number of laser photons absorbed). The emission rates themselves control n and subsequently $s \equiv \kappa \cdot k / \kappa \cdot q$, the lightfront momentum fraction. Given n , s and q , it is a matter of kinematics to determine k and then q' . Our Monte Carlo algorithm is as follows: (i) advance the electron trajectory by solving equations (12) and (13), (ii) evaluate, at every timestep, the probability of

emission and pseudorandomly decide whether to emit a photon or not, and on those timesteps where emission takes place, (iii) select a harmonic index n with probability W_n/W , where W_n is the partial rate and $W = \sum_{n=1}^{\infty} W_n$ is the total rate, (iv) sample s from the partial spectrum $(dW_n/ds)/W_n$, (v) determine k given n , s and q and (vi) reset the electron quasimomentum from q to q' .

The probability that emission takes place in small interval of lab time Δt is given by $\mathbf{P} = W\Delta\tau$ and $\Delta\tau = \Delta t(m/q^0)$ is the equivalent interval of proper time. We obtain W by integrating, and then summing, the partial, differential rates of emission W_n , which are given by [37]

$$\frac{dW_n}{ds} = -\alpha m \left\{ J_n^2(z) + \frac{a_{\text{rms}}^2}{2} \left[1 + \frac{s^2}{2(1-s)} \right] [2J_n^2(z) - J_{n-1}^2(z) - J_{n+1}^2(z)] \right\}. \quad (15)$$

The argument z of the Bessel functions J_n (of the first kind [66]) and auxiliary variables are

$$z^2 = \frac{4n^2 a_{\text{rms}}^2 s}{1 + a_{\text{rms}}^2 s_n(1-s)} \left[1 - \frac{s}{s_n(1-s)} \right], \quad s_n = \frac{2n\eta}{1 + a_{\text{rms}}^2} \quad (16)$$

and the bounds on s are $0 < s < s_n/(1 + s_n)$. Note that s_n depends on a_{rms} and η and is therefore a function of proper time τ , as shown explicitly in equation (10). While the summation should run from $n = 1$ to infinity, it is sufficient to sum up to a largest value $n_{\text{max}} = 10(1 + a_{\text{rms}}^3)$. In principle, the integration and summation can be done at every timestep, given the particular values of a_{rms} and η . However, it is significantly faster to obtain W by interpolating from a lookup table, where $W(a_{\text{rms}}, \eta)$ is precalculated over the domain $a_{\text{rms}}^{\text{min}} < a_{\text{rms}} < a_{\text{rms}}^{\text{max}}$ and $\eta_{\text{min}} < \eta < \eta_{\text{max}}$. The upper bounds are fixed by the problem space under consideration; we have taken $a_{\text{rms}}^{\text{max}} = 10$ and $\eta_{\text{max}} = 2$ in our code. The lower bounds are chosen such that alternative sampling strategies may be used.

First, if $a_{\text{rms}} < a_{\text{rms}}^{\text{min}} \ll 1$, only the first harmonic, $n = 1$, contributes significantly to the probability. In this limit, the rate may be obtained analytically:

$$W \simeq W_1 + O(a_{\text{rms}}^4), \quad W_1 = \frac{\alpha m a_{\text{rms}}^2}{2\eta} \left[\frac{2 + 8\eta + 9\eta^2 + \eta^3}{(1 + 2\eta)^2} - \frac{2 + 2\eta - \eta^2}{2\eta} \ln(1 + 2\eta) \right]. \quad (17)$$

Second, if $\eta < \eta_{\text{min}} \ll 1$, we may take the classical limit, whereupon the partial rates become:

$$\begin{aligned} \frac{dW_n}{dv} &\simeq \frac{\alpha m m \eta}{1 + a_{\text{rms}}^2} [a_{\text{rms}}^2 J_{n-1}^2(z) + a_{\text{rms}}^2 J_{n+1}^2(z) - 2(1 + a_{\text{rms}}^2) J_n^2(z)] + O(\eta^2), \\ z^2 &= \frac{4a_{\text{rms}}^2 n^2 v(1-v)}{1 + a_{\text{rms}}^2}, \end{aligned} \quad (18)$$

but where we fix $v = s(1 + s_n)/s_n$ to be $0 < v < 1$. Equation (18), integrated over $0 < v < 1$ and summed over $n = 1$ to n_{max} , is tabulated over the same range $a_{\text{rms}}^{\text{min}} < a_{\text{rms}} < a_{\text{rms}}^{\text{max}}$. In our implementation, $a_{\text{rms}}^{\text{min}} = 0.02$ and $\eta_{\text{min}} = 10^{-3}$. Thus at every timestep, the emission probability $\mathbf{P} = W\Delta\tau$ is obtained by interpolating from the appropriate lookup table, or using the limiting analytical expression. Emission is deemed to occur if a pseudorandom number R , drawn from the uniform distribution $U(0, 1)$, satisfies $R < \mathbf{P}$.

If emission takes place, the next step is to determine n and s . The former is obtained by solving for n , $R' = \sum_{i=1}^n W_i/W$, where R' is another pseudorandom number drawn on the unit interval $U(0, 1)$. In our implementation, the total rate of emission W is already available at this point; however, the sequence of partial rates must be evaluated explicitly, by integrating equation (15) over s . We do this, rather than store a lookup table in n (as well as in a_{rms} and η), because unlike the total rate, which is needed at every timestep, the partial rates are only needed on emission, which occurs at infrequent intervals. Once n is fixed, the lightfront momentum fraction transferred, s , is obtained by rejection sampling of equation (15).

The kinematical calculation of k is performed in the zero momentum frame (ZMF), which moves with four-velocity $u = (q + n\kappa)/[m\sqrt{1 + a_{\text{rms}}^2 + 2n\eta}]$ with respect to the lab frame. In the ZMF, the emitted photon has momentum $|\vec{k}_{\text{zmf}}| = mn\eta/\sqrt{1 + a_{\text{rms}}^2 + 2n\eta}$ and polar scattering angle $\cos \theta_{\text{zmf}} = 1 - s(1 + a_{\text{rms}}^2 + 2n\eta)/(n\eta)$. The azimuthal angle φ_{zmf} , which is arbitrary for circularly polarised backgrounds, is pseudorandomly determined in $0 \leq \varphi_{\text{zmf}} < 2\pi$. Once \vec{k}_{zmf} is determined, it may be boosted back to the lab frame, where q' follows from equation (14).

4. Benchmarking

While LMA rates have already been implemented in simulation codes used to study laser–electron interactions [34–36], the accuracy of these simulations has not been thoroughly benchmarked against the

underlying theory. Placing quantitative bounds on the error made, is essential for experiments that aim for precision characterisation of strong-field QED processes [13]. These analyses have been performed for LCFA-based simulations, however: see [29, 30, 67] and proposed improvements in [31–33]. In this section, we compare the results of simulations based on the LMA, as outlined in section 3, with QED theory calculations without the LMA, for photon emission in a pulsed, plane-wave background. We focus on the transition regime $a_0 \sim 1$, where currently existing approaches based on the LCFA are likely to fail. The laser pulses we consider are circularly polarised with a cosine-squared temporal envelope: the potential $\vec{a}(\phi) = a_0 f(\phi)[\vec{x} \cos b(\phi) + \vec{y} \sin b(\phi)]$, where $f(\phi) = \cos^2[\phi/(2N)]$ for $|\phi| < \pi N$. Here N is the number of cycles corresponding to the total duration of the pulse. One may estimate the (intensity) full-width-at-half-maximum duration of this pulse as $T[\text{fs}] \simeq N\lambda[\mu\text{m}]/0.8$. The function $b(\phi)$ controls the frequency chirping of the pulse and is initially set to $b(\phi) = \phi$ (i.e. unchirped) for the results in section IVA. The electrons counterpropagate head-on to the laser pulse, with initial energy parameter $\eta_0 = 0.1$. This is equivalent to an initial Lorentz factor of $\gamma_0 = 1.638 \times 10^4$ for a laser wavelength of $0.8 \mu\text{m}$.

The theoretical calculations described in section 2 are for *single* emission only. However, for sufficiently large a_0 or pulse length N , it is possible for the total probability of emission \mathbf{P} to exceed unity. This indicates that higher order processes, including the emission of multiple photons by a single electron, become important. Simulations model multiple emissions as the incoherent combination of single-vertex processes, transporting the electron classically between emission events. This is motivated by theoretical calculations of higher order processes which show that part of the probability can be factorised into a product over polarised, first-order processes [68–70]. Neglecting other contributions, where the intermediate state does not propagate, is expected to be a good approximation if $a_0^2 \Delta\phi \gg 1$ [71], where $\Delta\phi = 2\pi N$ is the phase duration of the pulse, which allows simulations to model cascades of photon emission and pair creation [60]. In the present case, we consider only the comparison for single photon emission results. Therefore, the probability obtained theoretically is interpreted as the average number of emitted photons [72]. As our simulations allow for an arbitrary number of emission events per electron, we obtain equivalent results by artificially disabling recoil, i.e. the electron momentum is not changed self-consistently when a photon is emitted. The number of emitted photons therefore scales exactly linearly with pulse duration. This does not apply to the theoretical results.

The symmetries of a plane wave suggest that the photon spectrum is best characterised in terms of the lightfront momentum fraction, s , and normalised perpendicular momentum $r_\perp = k_\perp/(ms)$. These provide proxies for the emitted photon energy ω' and polar scattering angle θ , respectively: $s = \omega'(1 + \cos\theta)/p^- \simeq \omega'/(m\gamma_0)$ and $r_\perp = (p^-/m)\tan(\theta/2) \simeq \gamma_0\theta$, where $p^- = m^2\eta_0/\omega_0$ is the initial lightfront momentum of the electron and γ_0 its Lorentz factor.

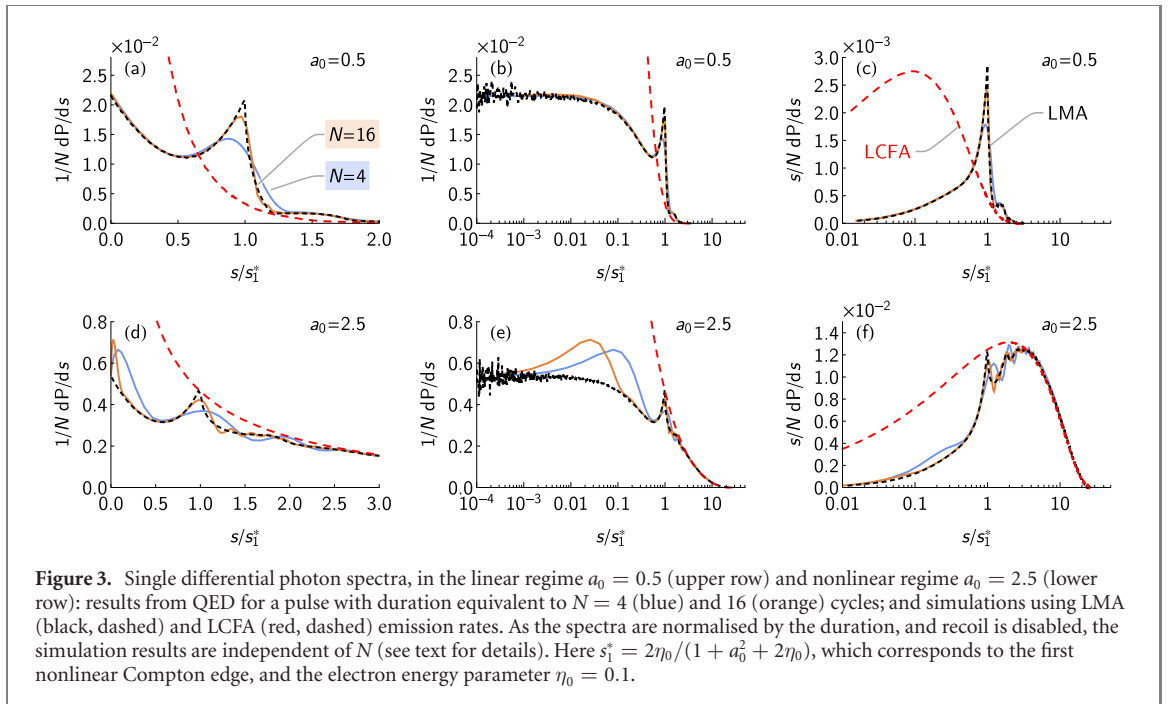
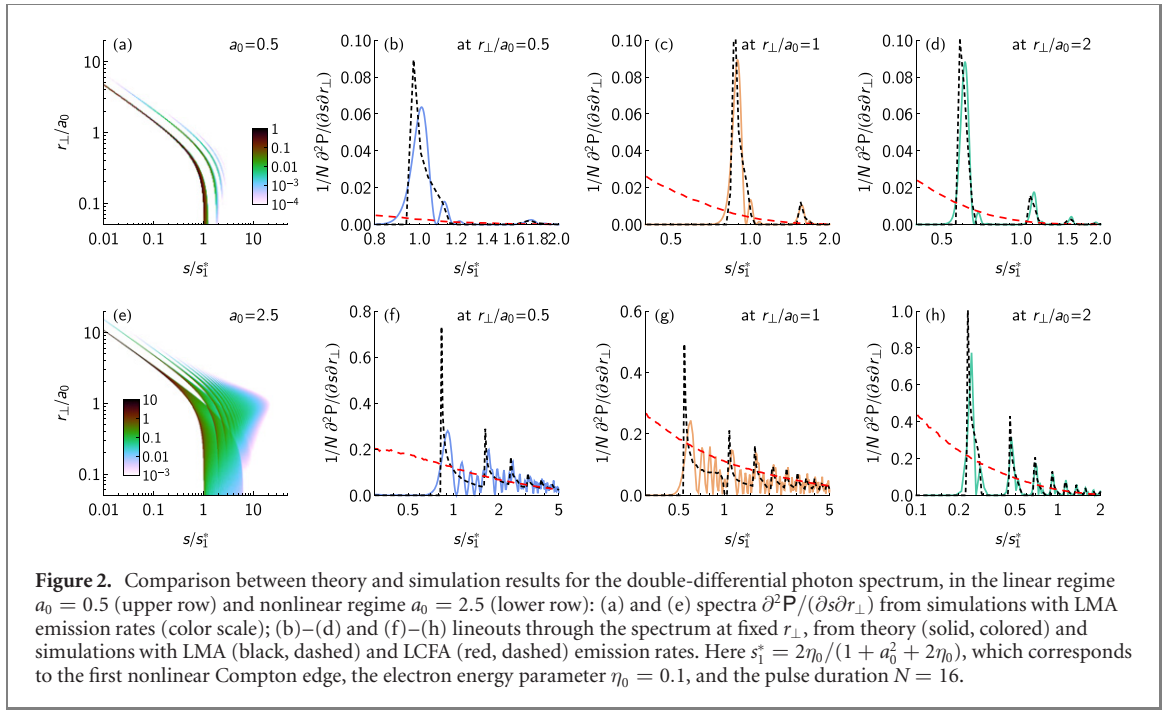
4.1. Pulsed plane waves

Figures 2(a) and (e) show photon spectra, double-differential in s and r_\perp , obtained from simulations in the linear and nonlinear regimes ($a_0 = 0.5$ and 2.5 respectively) for a pulse that is $N = 16$ cycles in duration. In the former case, radiation emission is dominated by the first harmonic, which displays the expected, characteristic energy–angle correlation. In the latter case, the radiation is composed of a broad range of high harmonics, extending the spectrum to much larger s . The effect of the pulse envelope is evident in the broadening of the first harmonic for small r_\perp : recall that the position of the first Compton edge, $s_1^* = 2\eta/(1 + a_{\text{rms}}^2 + 2\eta)$, is phase-dependent through a_{rms} and η . We also see that the higher harmonics are predominantly emitted at $r_\perp \simeq a_0$, as expected in the nonlinear regime, whereas for $a_0 = 0.5$, the characteristic $r_\perp < a_0$.

The three plots accompanying each double-differential spectrum compare lineouts at fixed r_\perp against theoretical results. The simulations capture the position and overall shape of the harmonics well, but miss the subharmonic substructure visible in figures 2(f) and (g) in particular. This structure arises from interference effects at the scale of the pulse envelope, whereas the LMA accounts only for interference effects at the scale of the wavelength. The LCFA, by contrast, captures neither, which causes the spectra to be smeared between the clear peaks seen in both the theory and LMA simulation results [29].

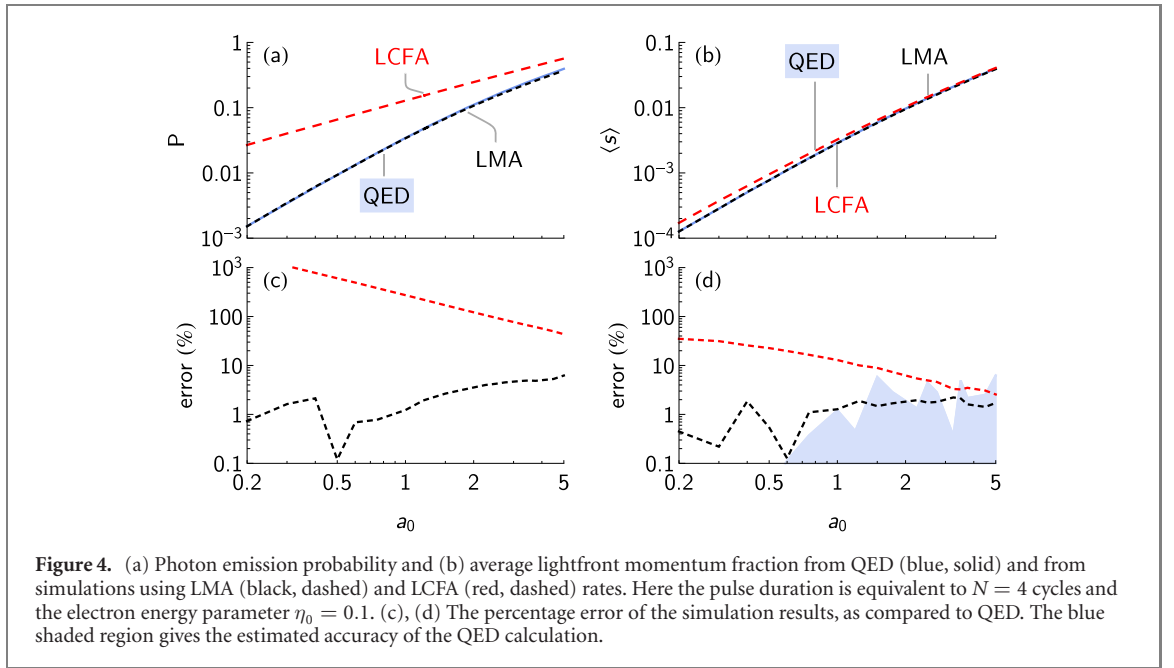
Single-differential spectra, i.e. the results from figure 2 integrated over r_\perp , are shown in figure 3. We compare the simulation results with QED for normalised amplitudes $a_0 = 0.5$ and 2.5 and for pulse durations equivalent to $N = 4$ and 16 cycles. The agreement is much better for the longer pulse, which we expect because the LMA neglects terms of order $1/N$ (see equation (8) and [37]). The LMA simulations capture the harmonic structure and correctly reproduce the small- s behavior of the theory, where the spectrum tends to a constant value $\propto a_0^2 \int f^2(\phi) d\phi$ [31, 37]. The LCFA simulations are significantly wrong in this region $s < s_1^*$, where we see the characteristic divergence $\propto s^{-2/3}$ [1].

The intermediate structure, which appears below the first Compton edge for $a_0 = 2.5$, shown in figure 3(e), is ponderomotive in origin: it is radiation from the slow decrease and increase of the electron



momentum caused by gradients in the intensity profile [73]. While this is accounted for at the level of the classical trajectory in the simulations, its contribution to the emission spectrum is neglected. The peak moves toward smaller s as N increases and it is eventually lost in the monochromatic limit [37]. Integrating over the s -weighted probability, shown in figures 3(c) and (e), yields the total lightfront momentum transfer from electron to photon. If $a_0 > 1$, this is dominated by contributions from $s > s_1^*$, where the LCFA works well [30]. However, it is evident from figure 3(c) that the LCFA fails globally for $a_0 < 1$.

Finally, we consider the total probability that a photon is emitted, \mathcal{P} , and the average lightfront momentum fraction of that photon, $\langle s \rangle \equiv \int s \frac{d\mathcal{P}}{ds} ds$, as a function of a_0 for a four-cycle pulse. The values obtained from theory and from LMA and LCFA simulations are shown in figure 4, along with the percentage error made by the simulations. The LMA-based simulations are accurate at the level of a few per cent across the full range of a_0 explored. The improvement over the LCFA is particularly dramatic for the probability, where the error made is larger than 10% even when $a_0 = 5$. The average lightfront momentum fraction is more sensitive to the contribution of higher harmonics, i.e. large s ; as this is where the LCFA



works rather well, the accuracy for $\langle s \rangle$ is better than that for P . However, the LMA simulations are significantly more accurate when $a_0 \lesssim 1$.

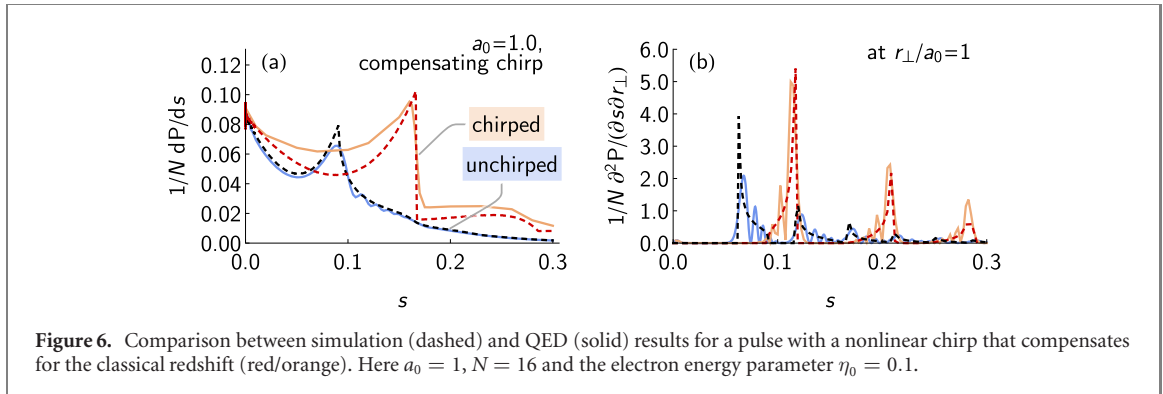
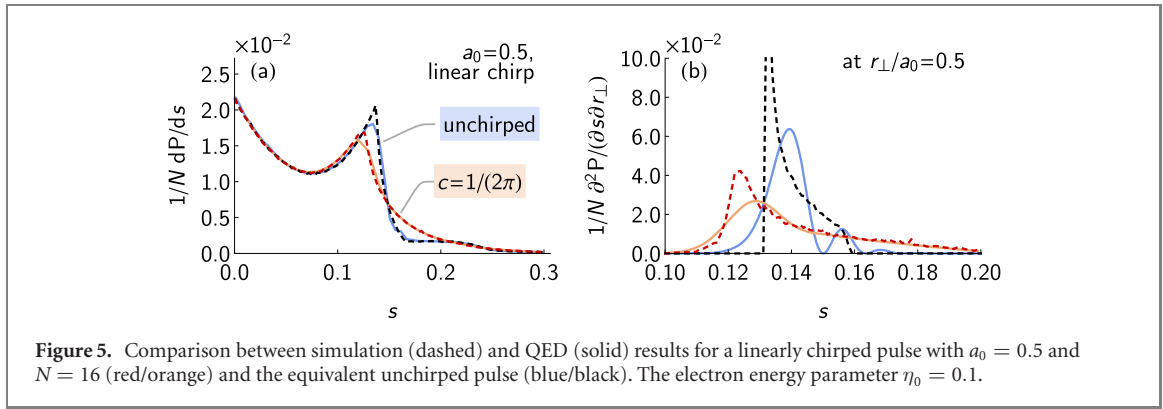
4.2. Chirped pulses

In Heinzl *et al* [37], the LMA is derived for a pulse in which the amplitude is slowly varying. However, a monochromatic plane wave is defined by both an amplitude and a frequency. By extending the LMA to the situation where both may vary with phase, it becomes possible to simulate radiation generation in chirped laser pulses in the transition regime $a_0 \sim 1$. In this section we benchmark our simulation results against theory for this case.

The first example we consider is that of a linearly chirped laser pulse, which has potential $\vec{a}(\phi) = a_0 f(\phi) [\vec{x} \cos b(\phi) + \vec{y} \sin b(\phi)]$, where $f(\phi) = \cos^2[\phi/(2N)]$ for $|\phi| < \pi N$ and $b(\phi) = \phi[1 + c\phi/(2N)]$. The instantaneous frequency, $\omega(\phi) = \omega_0(1 + c\phi/N)$ for chirp parameter c , must be positive throughout the pulse, which imposes the restriction $c < 1/\pi$. This is consistent with the condition for the chirp to be slowly varying, equation (8), which may be cast as $c \ll N/(1 + \pi N)$. Furthermore, for a particular pulse duration, there is an upper bound on the largest chirp that can be obtained [74]. In our notation, this maximum is given by $\chi r p_{\max} \simeq 10/N$. We note that chirping a pulse, which is accomplished by introducing a frequency-dependent phase shift, also changes its duration and peak amplitude; we neglect these such that the only difference between the chirped and unchirped case is the variation of the instantaneous frequency.

We compare the photon spectra obtained from theory and LMA-based simulations for $a_0 = 0.5$, $N = 16$ and $c = 1/(2\pi)$ in figure 5. The unchirped results, $c = 0$, are also shown for reference. The theoretical results are obtained numerically, using equation (6) and the explicit form of the potential $\vec{a}(\phi)$. For this case, the electron trajectory can be written in a closed form in terms of Fresnel functions. In the simulations, a chirp is included by promoting the frequency of the background κ^μ to be a function of phase $\kappa^\mu(\phi)$. We find that the simulations capture the softening of the harmonic structure evident in the theory results for the chirped pulse. Lineouts through the theoretical double-differential spectrum at fixed r_\perp demonstrate that chirping smooths out the subharmonic structure; as a consequence, simulation results appear to be more accurate than in the unchirped case.

The second example we present is that of a highly nonlinear chirp, where the instantaneous frequency varies in such a way as to compensate for the classical broadening of the photon spectrum at $a_0 > 1$. In a pulsed plane wave, the position of the first harmonic edge varies from $s = 2\eta_0/(1 + 2\eta_0)$ to $s = 2\eta_0/(1 + a_0^2 + 2\eta_0)$ as the cycle-averaged potential $a_{\text{rms}}(\phi)$ sweeps up and down. As such, the on-axis emission is broadband unless the intensity is rather low. In order to overcome this, and obtain a narrowband source of Compton γ rays even when a_0 is not small, it has been proposed to chirp the pulse in a particular way [75–79]. If the instantaneous frequency of the pulse varies as $\omega(\phi) = \omega_0[1 + a_{\text{rms}}^2(\phi)]$, then $s = 2\eta_0/(1 + 2\eta_0)$ for all ϕ and the nonlinear redshift is perfectly compensated. Although there are significant obstacles to achieving this in experiment, it is a useful test case for the simulation method we



have introduced. We therefore consider a pulse with envelope $f(\phi) = \cos^2[\phi/(2N)]$ for $|\phi| < \pi N$ and $b(\phi) = \phi + a_0^2 \int_0^\phi f^2(y) dy$. In this case, the chirp may be considered to be slowly varying if $2a_0^2/[N(1+a_0^2)] \ll 1$. We show results for $a_0 = 1$, $N = 16$ in figure 6. The lightfront momentum spectrum for theory and simulation both show a shift of the edge of the first harmonic from the nonlinear, to the linear position, as expected for this choice of chirp. However, this rather extreme choice of chirp leads to a larger discrepancy in the in the height of the spectra: the simulations underestimate the total yield by a small but not insignificant amount. We have verified that both theory curves tend to the same value in the limit of vanishing s , and that the simulation curves do as well: the limiting value, $\lim_{s \rightarrow 0} \frac{dP}{ds} \propto a_0^2 \int f^2(\phi) d\phi$, is sensitive only to the pulse *envelope* (for circular polarization) [31, 37].

5. Focused lasers

Theoretical calculations of strong-field QED effects in experimentally relevant scenarios must deal with three-dimensional effects: the nonlinear regime $a_0 \gtrsim 1$ is reached by focusing laser light to a spot of small, even diffraction-limited, size, so the laser pulse will differ significantly from a plane wave; the electron beam that probes the laser will also have finite size and temporal duration. Theoretical results build upon analytical solutions of the Dirac equation in a background field and are therefore only available for plane waves, focusing models of very high symmetry [43, 44], or under a high-energy approximation $\gamma \gg a_0$ [45, 47]. In this section, we discuss the application of simulations, based on LMA emission rates, to model the interaction of electron beams with focused laser pulses.

Within the LMA, the field is treated locally as a monochromatic plane wave. In order to model a focused laser pulse, we therefore promote the cycle-averaged amplitude a_{rms} and wavevector κ to be functions of spatial coordinate as well as phase. For Gaussian focusing, within the paraxial approximation, we have

$$a_{\text{rms}} = \frac{a_0 f(\psi)}{\sqrt{1 + \zeta^2}} \exp\left(-\frac{\rho^2}{1 + \zeta^2}\right), \quad \rho^2 = \frac{x^2 + y^2}{w_0^2}, \quad \zeta = \frac{z}{z_R}, \quad (19)$$

where w_0 is the beam waist (the radius at which the intensity falls to $1/e^2$ of its central value), $z_R = \pi w_0^2/\lambda$ is the Rayleigh range, and the factor $f(\psi)$ is the pulse envelope [80]. The local wavevector $\kappa_\mu = \partial_\mu \psi$, where $\psi = \phi - \rho^2 \zeta / (1 + \zeta^2) + \tan^{-1} \zeta$ is the total phase. However, in what follows we neglect the wavefront curvature and Gouy phase so that $\psi = \phi$ and κ takes its usual, plane-wave value. We compare the results so obtained with simulations based on the LCFA, which is a more standard approach [15, 16]. In the LCFA

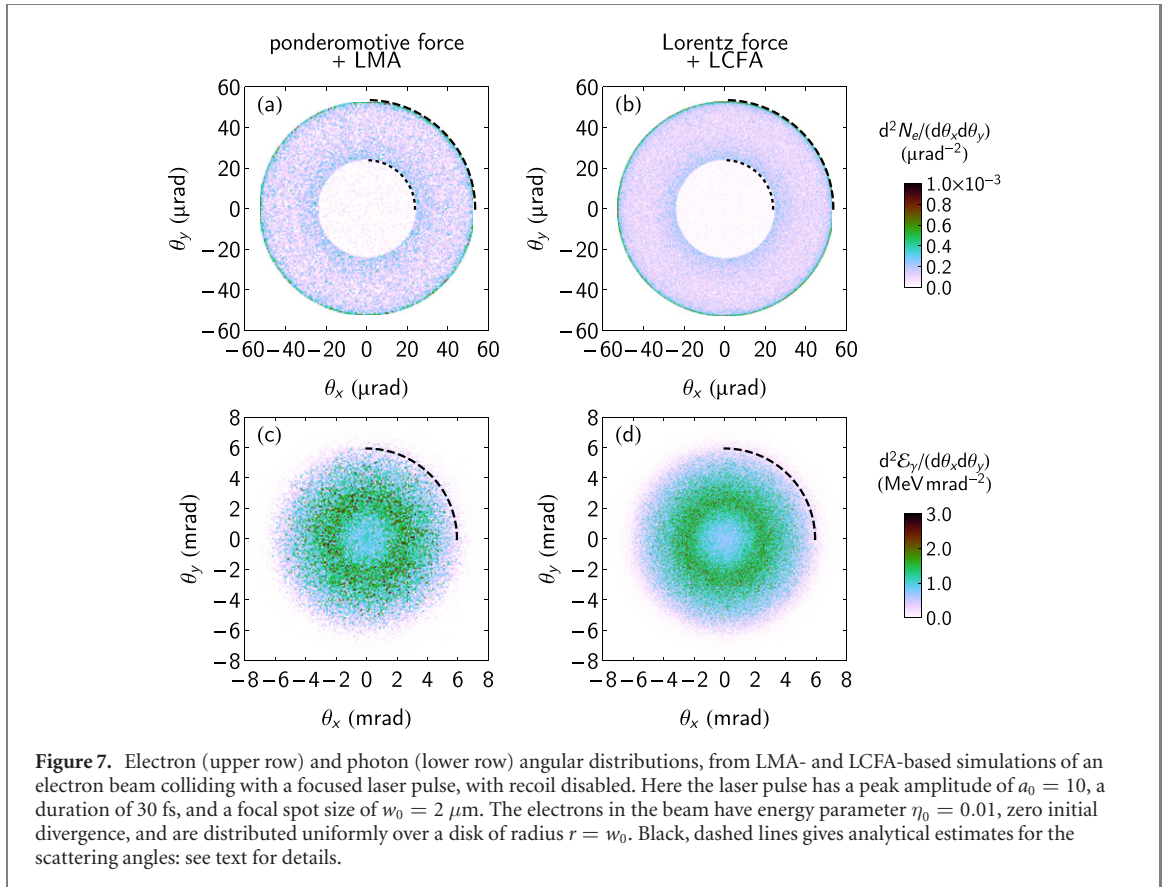


Figure 7. Electron (upper row) and photon (lower row) angular distributions, from LMA- and LCFA-based simulations of an electron beam colliding with a focused laser pulse, with recoil disabled. Here the laser pulse has a peak amplitude of $a_0 = 10$, a duration of 30 fs, and a focal spot size of $w_0 = 2 \mu\text{m}$. The electrons in the beam have energy parameter $\eta_0 = 0.01$, zero initial divergence, and are distributed uniformly over a disk of radius $r = w_0$. Black, dashed lines gives analytical estimates for the scattering angles: see text for details.

simulations, the laser pulse is defined using the paraxial solution for the fields given in [81]: we include terms up to fourth-order in the diffraction angle $\varepsilon = w_0/z_R$ in the Gaussian beam, which is then multiplied by a temporal envelope $f(\phi)$. Electron trajectories are determined by solution of the ponderomotive force equation, equation (12), for the quasimomentum, or the Lorentz force for the kinetic momentum, as appropriate.

First, we verify that LMA and LCFA simulations yield consistent results in a regime where they are expected to do so. We consider a laser pulse that is focused to a spot size $w_0 = 2 \mu\text{m}$, reaching a peak amplitude of $a_0 = 10$, with Gaussian temporal envelope of (full width at half maximum) duration 30 fs. The electrons have initial energy parameter $\eta_0 = 0.01$ (equivalent to $\gamma_0 = 1638$, given a laser wavelength of $0.8 \mu\text{m}$) and are initially counterpropagating, with zero initial divergence. Their initial positions are distributed over a disk of radius $r_0 = w_0$, such that they encounter a range of peak intensities. We have both $a_0 \gg 1$ and $a_0^2/\eta_0 \gg 1$, so the LCFA is expected to be a good approximation. The results presented in figure 7 are obtained from simulations of this scenario using the LMA and LCFA, with recoil on photon emission artificially disabled. This means that the electron trajectory is determined solely by the action of the laser fields, allowing us to confirm the equivalence between the LMA and LCFA at the level of the electron dynamics, illustrated in figure 1.

Figure 7 shows the angular distributions of the electrons and emitted photons, after the collision has taken place. We see immediately that the LMA and LCFA simulations yield almost identical results. In order to explain the double ring structure evident in the electron distributions, we derive an approximate, analytical prediction for the expected ponderomotive scattering angle³. Consider an electron that is initially counterpropagating, with no initial transverse momentum, at radial distance (impact parameter) b from the laser axis, at ultrarelativistic velocity such that $q^0 \simeq -q^3 \gg q^\perp$. We approximate $a_{\text{rms}}^2 \simeq [a_0 \exp(-r^2/w_0^2) f(\phi)]^2$ and solve the equation of motion, equation (12), perturbatively in the small parameter $\epsilon \equiv 1/\gamma_0$. The first-order correction to the perpendicular momentum q^\perp is obtained by substituting into equation (12) $q^0 = m\gamma_0$ and $r = b$, i.e. assuming the electron is undeflected. The deflection angle follows as

³ Analytical predictions for the scattering angle are also given in [82], but these are derived under the assumptions that the laser transverse intensity profile is flat up to a radius equal to the waist, and that the pulse duration is infinitely long. Neither condition applies here.

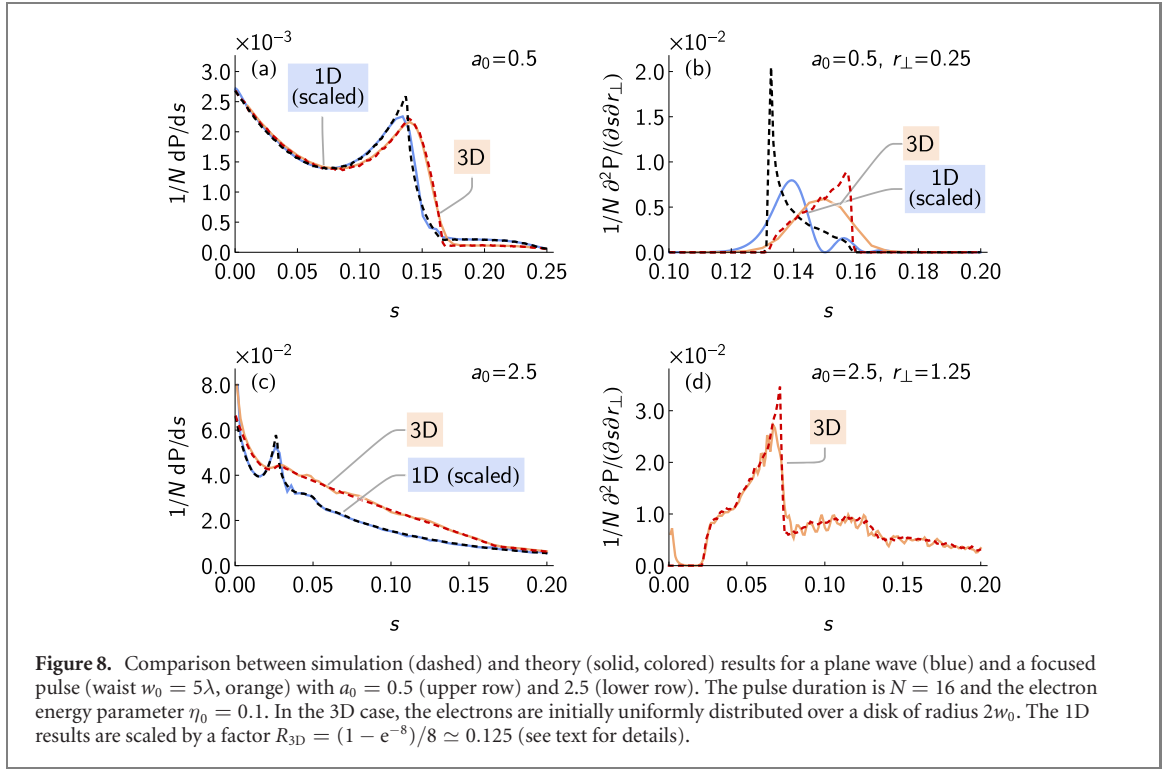


Figure 8. Comparison between simulation (dashed) and theory (solid, colored) results for a plane wave (blue) and a focused pulse (waist $w_0 = 5\lambda$, orange) with $a_0 = 0.5$ (upper row) and 2.5 (lower row). The pulse duration is $N = 16$ and the electron energy parameter $\eta_0 = 0.1$. In the 3D case, the electrons are initially uniformly distributed over a disk of radius $2w_0$. The 1D results are scaled by a factor $R_{3D} = (1 - e^{-8})/8 \simeq 0.125$ (see text for details).

Table 2. Conditions on the pulse amplitude a_0 , phase duration $\omega_0\tau$ and electron energy parameter $\eta = \kappa \cdot p/m^2$ for simulated photon yields and spectra to be accurate under the LMA and LCFA.

Predicted quantity	LCFA is accurate when	LMA is accurate when
Yield, N_γ	$a_0^2/\eta \gg 1, a_0 \gg 1, \omega_0\tau \gg 1^a$	$\omega_0\tau \gg 1$
Spectrum, $\frac{dN_\gamma}{ds}$	$s \gtrsim \frac{2\eta}{1+a_0^2+2\eta}$	$s \gtrsim s_0^*, s \ll s_0^*$ where $s_0^* = \frac{\eta/N}{1+a_0^2+\eta/N}$

^aThe last condition expresses that the photon formation length should be smaller than both the wavelength λ and the pulse length τ . It follows from the standard LCFA applicability conditions $[(a_0^2/\eta)s/(1-s)]^{1/3} \gg 1$ and $a_0 \gg 1$, when one chooses $s = s_0^*$ and $\eta \ll Na_0^2$, corresponding to the mid-IR peak.

$$\theta \simeq q^\perp/q^0:$$

$$\theta_e \simeq \frac{a_0^2}{\gamma_0^2} \frac{be^{-2b^2/w_0^2}}{z_R} \int_{-\infty}^{\infty} f^2(\phi) d\phi. \quad (20)$$

The outer ring in figures 7(a) and (b) corresponds to scattering at $b = w_0/2$ (shown by the black, dashed line), at which equation (20) is maximised, and the inner ring to scattering at $b = w_0$ (shown by the black, dotted line), which is the radius of the electron beam.

As discussed in section 3, and shown in figure 1, angular structure in the photons emerges differently in the LMA and LCFA simulations. In the former, it is the emission rate and the conservation of quasimomentum that ensures that photons are most probably emitted at angles $\theta_\gamma \simeq a_0/\gamma_0$ to the instantaneous quasimomentum. In the latter, it arises from the instantaneous oscillation in the electron kinetic momentum, which has characteristic angle $\theta_e \simeq a_0/\gamma_0$, and the fact that the radiation is beamed parallel to this. The azimuthal symmetry of a circularly polarised laser means that the radiation angular profile is annular in shape: while this is evident in figures 7(c) and (d), the characteristic angle is smaller than the expected value $\theta_\gamma = a_0/\gamma_0$, which is shown by the black, dashed line. This is caused by the fact that the electrons are distributed over a range of impact parameters and therefore encounter lower effective values of a_0 : $a_0^{\text{eff}}(b) \simeq a_0 \exp(-b^2/w_0^2)$.

Focal spot averaging not only lowers the yield of photons, as compared to a plane wave with the same peak amplitude, it also reduces the clarity of signatures of strong-field QED effects. We demonstrate this in particular for the position of the first nonlinear Compton edge, at $a_0 \sim 1, \eta_0 = 0.1$. This also provides an opportunity to crosscheck our LMA simulation results for focused lasers with theory. The latter is obtained using equation (11), i.e. under the high-energy approximation that the electron is undeflected during its passage through the laser pulse. We have already shown that the total deflection angle scales as $(a_0/\gamma_0)^2$, which is indeed very small. In this case, the laser amplitude is either $a_0 = 0.5$ or 2.5 , its waist is $w_0 = 4 \mu\text{m}$,

and its temporal envelope (electric-field) is $f(\phi) = \cos^2[\phi/(2N)]$ with $N = 16$. The electrons have energy parameter $\eta_0 = 0.1$ (equivalent to $\gamma_0 = 1.638 \times 10^4$ for a head-on collision with a laser pulse of central wavelength $\lambda = 0.8 \mu\text{m}$) and are distributed uniformly over a disk of radius $2w_0$.

In figure 8, we compare the theory and simulation results with those obtained for a plane wave with the same peak amplitude. As the total yield is reduced in the former case, we scale the plane-wave results by a factor R_{3D} which approximately accounts for the effect of focal spot averaging. In the perturbative limit $a_{\text{rms}} \ll 1$, the emission rate is proportional to a_{rms}^2 . Thus we expect the overall number of photons, in the 3D case, to be reduced by a factor $R_{3D} \simeq (\int a_{\text{rms}}^2(b) \frac{dN_c}{db} db) / a_0^2$, where $\frac{dN_c}{db}$ is the distribution of electron impact parameters b , and we may take $a_{\text{rms}}(b) = a_0 \exp(-b^2/w_0^2)$ for beam waist w_0 . For a beam of electrons which are uniformly distributed over a disk of radius $2w_0$, we have $R_{3D} = (1 - e^{-8})/8 \simeq 0.125$. The distribution of photon lightfront momentum fraction s is shown in figures 8(a) and (c) for $a_0 = 0.5$ and 2.5 respectively. Figures 8(b) and (d) show lineouts through the double-differential spectrum at fixed $r_{\perp} = a_0/2$. The agreement between theory and simulation is reasonably good. The detailed structure in the lineouts is not resolved, because the LMA misses interference effects at the scale of the pulse envelope. This is more evident in figure 8(b) than figure 8(d), i.e. at lower a_0 , for the following reason. In the LMA, the only contribution to the bandwidth of an individual harmonic is the variation in the mass shift over the pulse duration: at fixed r_{\perp} , this width is $\Delta s/s = a_0^2/(1 + 2m\eta)$. There is an additional contribution from the non-zero bandwidth of the pulse, which is given approximately by $\Delta s/s \simeq 0.187/(\omega_0\tau)$, where τ is the FWHM duration of the pulse intensity profile: for the cosine-squared envelope under consideration here, $\omega_0\tau \simeq 0.364N$ and $\Delta s/s \simeq 1/(2N)$. At sufficiently small a_0 , it is the latter contribution, from the laser pulse bandwidth, that dominates. Note that in a focused pulse, the effective amplitude at finite impact parameter $a_{\text{rms}}(b) < a_0$ and so such effects are magnified. Integrating over a finite range of r_{\perp} partially mitigates this, which is why the single-differential spectra are in much better agreement.

The difference between the 1D and 3D cases, evident in the theory, is captured very well by the simulations. We see that the first nonlinear edge is smeared out by focal spot averaging, particularly for $a_0 = 2.5$. This is because the position of the edge differs for electrons at different impact parameters, as increasing b means reducing the effective a_0 . We have repeated the comparison between LMA-based simulations and QED for more tightly focused laser pulses, reducing the waist w_0 to 3λ and 1λ , while holding the peak a_0 and the electron-beam–laser overlap fixed. The detailed results are shown in the supplementary material (<https://stacks.iop.org/NJP/23/085008/mmedia>): we find that the spectra are barely affected by the reduction and the agreement between simulations and theory is consistently good. This supports our expectations that LMA-based simulations are accurate even for focused laser pulses.

6. Discussion

The focus of this paper has been incorporating the LMA into numerical simulation and providing the first benchmarks for a range of parameters and observables with direct calculation from QED. As part of this work, we compare the LMA to the LCFA, which is the standard scheme for including QED effects in the modeling of intense laser interactions. The power of the LCFA is, in part, due to its versatility. It can be used when the strong electromagnetic field is not known *a priori*, which is a particular advantage when dealing with a laser–plasma interaction. However, in situations where the shape of the intense laser pulse is well-known, and unchanged in the interaction, the LMA can be used to attain a higher precision than the LCFA. The demand for the precision is acute if the field strength and particle energies in question are outside the region of validity of the LCFA, as is the case in some upcoming high-energy experiments [12, 13].

Using a plane-wave pulse with phase duration $\omega_0\tau = 2\pi N$, we can give some indication for parameter regimes where the approximations can be used. We designate the region of accuracy as being when particle and field parameters are far away from values where it is known that the approximation is in doubt. We summarize our findings in table 2 for the photon yield and spectrum separately, as the conditions depend on the quantity that is to be measured. Note that, for these two quantities, the ‘penalty’ from violating the validity conditions is not equal in each case: if the LCFA is used to calculate the yield outside of the range given by a_0 and η , the prediction can be wrong by orders of magnitude (as demonstrated by figure 4). The requirement that $\omega_0\tau \gg 1$ for the LMA to be accurate is softer. Figure 4 shows that the simulations are accurate to within a few per cent even if $N = 4$, which is already much shorter than most typical laser pulses (where the equivalent $N \gtrsim 10$): furthermore we expect the accuracy to improve with increasing N . Similarly, the error made by the LCFA in the photon spectrum becomes arbitrarily large as $s \rightarrow 0$, even if $a_0 \gg 1$, whereas the LMA is guaranteed to obtain the correct limiting value for all a_0 . The LMA result is inaccurate only in a small region around $s \simeq s_0^* = (\eta/N)/(1 + a_0^2 + \eta/N)$ [73], which is in any case missed by the LCFA: radiation here arises from the slow ponderomotive scattering of the electron.

If the plane wave contains a chirp, then the condition that the LMA is still a good approximation is found to be $|\omega'/\omega| \ll 1$, which is a ‘slowly varying’ condition of the same nature as $1/N \ll 1$. In practice, one is often limited to such chirps by virtue of the available bandwidth [74]. For focused laser pulses, we may expect that the applicability regime apparent when a chirp was introduced, should be adaptable for the change in wave vector \vec{k} obeying $|\vec{k}'|/|\vec{k}| \ll 1$. This reduces to a condition on the focusing, which may be expressed through the diffraction angle $\varepsilon = \lambda/(\pi w_0)$ as $\varepsilon \ll 1$. (A similar condition applies to the validity of the ponderomotive-force approach to the particle’s classical dynamics [64], which confirm for $\varepsilon \simeq 0.12$ in figure 8.) Using the high-energy approximation with the focused background in equation (19), we note $z/z_R = -\phi/(2\omega z_R)$, and the relevant change in wave-vector on the focal axis is $k'/k \sim 1/(\omega z_R) = \varepsilon^2/2 \ll 1$. We have cross-checked our simulation results against a theoretical calculation which uses a WKB approximation, suitable for high-energy electrons. This integrates the plane-wave probability over a transverse distribution of intensity and particle flux and therefore works in a similar way to our simulations. We find good agreement even for diffraction-limited focal spots (see supplementary material), when $|\vec{k}'|/|\vec{k}| \ll 1$ still holds. To benchmark the LMA fully would require solutions to the Dirac equation in backgrounds beyond a plane wave, which is still an active area of research [43, 83, 84].

7. Summary

Motivated by the imminent need for precision simulations of strong-field QED processes in the transition regime $a_0 \sim 1$, we have presented here a novel simulation framework which incorporates quantum effects via probability rates calculated within the LMA [37]. From the theory perspective, the formalisation of the LMA from the plane-wave model has been extended to include chirped pulses, under a ‘slowly varying chirp’ approximation. We have also adapted the LMA to model focused laser backgrounds, under the approximation that the incident electron has a relativistic γ factor satisfying $\gamma \gg a_0$.

The emission rates so derived are embedded within a classical simulation framework that assumes a definite particle trajectory. In contrast to simulations based on the LCFA, the electron quasimomentum (the cycle-averaged kinetic momentum) plays the essential role here, appearing in the classical equations of motion and the conservation of momentum. The fast oscillation of the particle momentum, at the timescale of the laser frequency, is nevertheless included, but at the level of the emission rates. This simulation framework therefore has conceptual similarities to the ‘envelope solvers’ used to model laser-wakefield acceleration [85–87].

In benchmarking the simulations against QED results, we have found excellent agreement for a variety of background field configurations. Furthermore, we obtain significant reductions in the relative error when compared to the use of the LCFA in the transition regime. While we have focused, in this work, on the specific example of nonlinear Compton scattering in a circularly polarised background, our results can be extended to other processes, such as electron–positron pair creation [1,37], and to include spin- and polarisation-dependence [88–92].

Acknowledgments

We would like to thank members of the LUXE collaboration for helpful discussions during preparation of this work. We acknowledge funding from the Engineering and Physical Sciences Research Council (Grant EP/S010319/1, BK, AJM). Simulations were performed on resources provided by the Swedish National Infrastructure for Computing at the High Performance Computing Centre North.

Data availability

The source code for the simulation program described is available at reference [93]. Version 0.6.0, which is used in this work, the input configurations necessary to reproduce the simulation results, and the analytical results, are archived at reference [94].

Appendix A. Locally monochromatic approximation for general chirped plane-wave pulses

In [37], the LMA was derived from plane-wave QED for a simple plane-wave pulse. A plane wave is a highly idealised model of a laser field, which does not take into account some of the important characteristics of pulses in a real experiment. Here we extend the LMA to the case of a plane-wave pulse which includes an

arbitrary chirp. We begin with a general overview of the LMA for a plane-wave field with a general chirp term.

For concreteness, we use a circularly polarised pulse with an arbitrary chirp, where the dimensionless gauge potential $a_\mu(\varphi) = eA_\mu(\varphi)/m$ is

$$a_\mu(\phi) = a_0 f\left(\frac{\varphi}{\Phi}\right) [\varepsilon_\mu \cos b(\varphi) + \beta_\mu \sin b(\varphi)], \quad (\text{A1})$$

and the phase is $\varphi = \kappa \cdot x$. In the derivation of the LMA, it is more natural to work with functions of the phase variable φ , than the proper time τ , which is used in the main text, and so in what follows we work with φ . The discussion here can be generalised to linearly or elliptically polarised backgrounds (see [37] for more details on the subtleties involved in the LMA for a linear, unchirped, plane-wave pulse).

We follow the standard approach of defining the scattering amplitude for our process in terms of the Volkov wavefunctions for the background dressed fermions of mass m and four-momentum p_μ , [55],

$$\Psi_{p,r}(x) = \left(1 + \frac{m \not{\kappa} \not{a}(\varphi)}{2\kappa \cdot p}\right) u_{p,r} e^{-iS_p(x)}, \quad (\text{A2})$$

where u_p are constant spinors. The Volkov phase term is given by,

$$S_p(x) = p \cdot x + \int_{-\infty}^{\varphi} dy \frac{2m p \cdot a(y) - m^2 a^2(y)}{2\kappa \cdot p}, \quad (\text{A3})$$

which is just the classical action for an electron in a plane-wave background field. The nontrivial dependence of the Volkov wavefunctions on the phase φ means that overall momentum conservation for an arbitrary scattering amplitude \mathbf{S} in the plane-wave background field only holds for three of the four directions, $\{-, \perp\}$. As such, the scattering amplitude takes the form,

$$\mathbf{S} = (2\pi)^3 \delta_{-,\perp}^3(p_{\text{in}} - p_{\text{out}}) \mathcal{M}, \quad (\text{A4})$$

where $\delta_{-,\perp}^3(p) = \delta(p_-) \delta(p_\perp) \delta(p_\parallel)$, and \mathcal{M} is the invariant amplitude.

Closed form solutions to equation (A3) are not always available. A simple example is the infinite monochromatic plane wave, which is the $f(\varphi/\Phi) \rightarrow 1$, $b(\varphi) \rightarrow \varphi$ limit of the background field equation (A1). However, one can separate the fast and slow dynamics of the background field in such a way that the field dependent terms in the exponent can be integrated by parts, and simplified by neglecting derivative corrections. This technique is known as the slowly varying envelope approximation [37–41].

The slowly varying envelope approximation for an arbitrarily chirped plane-wave field was derived in [58], and we follow this approach here. For the circularly polarised background equation (A1), the terms which are quadratic in the field depend only on the slowly varying envelope, $a^2(\varphi) = -a_0^2 f^2(\varphi/\Phi)$, while the terms linear in the field contain both slow (through f) and fast (through b) timescales. This gives integrals of the form,

$$\mathcal{I} = \int_{-\infty}^{\varphi} dy f\left(\frac{y}{\Phi}\right) [\cos b(y), \sin b(y)]. \quad (\text{A5})$$

To deal with these integrals, we first transform the trigonometric functions of $b(y)$ to pull out a factor depending on the inverse of $\omega(y) = b'(y)$, where a prime denotes a derivative of the argument:

$$\mathcal{I} = \int_{-\infty}^{\varphi} dy \frac{f(y/\Phi)}{\omega(y)} \frac{d}{dy} [\sin b(y), -\cos b(y)]. \quad (\text{A6})$$

The function $\omega(y)$ is taken to define a *local frequency scale*. Each term can then be readily integrated by parts, giving two contributions: a boundary term and a term proportional to

$$\frac{d}{dy} \frac{f(y/\Phi)}{\omega(y)} = \frac{1}{\Phi} \frac{f'(y/\Phi)}{\omega(y)} - \frac{f(y/\Phi)}{\omega^2(y)} \omega'(y). \quad (\text{A7})$$

Provided this is a small correction, which is valid for sufficiently long pulses, $\Phi \gg 1$ and when the derivative of the chirp function satisfies $\omega'(y) \ll \omega(y)$, we can neglect these slowly varying terms, and approximate the integrals by,

$$\mathcal{I} \simeq \frac{f(\varphi/\Phi)}{\omega(\phi)} [\sin b(\varphi), -\cos b(\varphi)]. \quad (\text{A8})$$

Applying these approximations to the classical action S_p in equation (A3) gives,

$$S_p(x) = G(\varphi) - z(\varphi) \sin[b(\varphi) - \vartheta]. \quad (\text{A9})$$

The function $G(\varphi)$ contains only slowly varying terms, or terms linear in φ . The function $z(\varphi)$ depends on the phase only through the slowly varying envelope $f(\varphi/\Phi)$ and local frequency $\omega(\varphi)$, and the angle ϑ is *independent* of the phase.

The exponential of the trigonometric function in equation (A9) can be expanded into an infinite sum of Bessel functions using the Jacob–Anger expansion,

$$e^{-iz \sin(b-\vartheta)} = \sum_{n=-\infty}^{\infty} e^{-in(b-\vartheta)} J_n(z). \quad (\text{A10})$$

For the case of a one vertex process, such as nonlinear Compton scattering or Breit–Wheeler pair production, once the oscillating phase term has been expanded by equation (A10), the invariant amplitude, \mathcal{M} , in equation (A4), takes on the form,

$$\mathcal{M} = \int d\varphi \sum_{n=-\infty}^{\infty} \mathcal{M}'_n(\varphi). \quad (\text{A11})$$

The probability, \mathbf{P} , is then found in the usual way by squaring the scattering amplitude equation (A4) and integrating over the Lorentz invariant phase space for the particular process, $d\Omega_{\text{LIPS}}$,

$$P \propto \iint d\varphi d\varphi' \sum_{n,n'=-\infty}^{\infty} \int d\Omega_{\text{LIPS}} \mathcal{M}'_n{}^\dagger(\varphi) \mathcal{M}'_{n'}(\varphi'). \quad (\text{A12})$$

There are now two phase integrals, and what distinguishes the LMA from the slowly varying approximation (which is all we have applied so far) is performing a local expansion in the phase variables. To achieve this we introduce the sum and difference variables,

$$\phi = \frac{1}{2}(\varphi + \varphi'), \quad \theta = \varphi - \varphi', \quad (\text{A13})$$

and then take the small phase difference approximation $\theta \ll 1$ to expand the probability in a Taylor series in θ , retaining only the leading-order, $O(\theta)$, contributions.

The θ -integral can be performed analytically, leaving the probability in the form,

$$\mathbf{P}^{\text{LMA}} = \int d\phi \mathbf{R}^{\text{LMA}}(\phi). \quad (\text{A14})$$

The function, $\mathbf{R}^{\text{LMA}}(\phi)$, contains summations over the Bessel harmonics and integrations over the final states, but crucially only depends on *one* phase variable. This allows us to interpret $\mathbf{R}(\phi)$ as a *local rate* which can be used in simulations. (In the main paper, we instead use a rate W^{LMA} defined as a probability per unit proper time.) To make this discussion more explicit, we consider the process of nonlinear Compton scattering.

A.1. Nonlinear Compton scattering in a chirped plane-wave pulse

Consider an electron with an initial momentum p_μ interacting with a plane-wave electromagnetic field to produce a photon of momentum k_μ and polarisation $\epsilon_{k,l}^*$. The scattering amplitude, in terms of the Volkov wave functions equation (A2), is given by,

$$\mathbf{S}_{r',r;l} = -ie \int d^4x \bar{\Psi}_{p',r'}(x) \not{\epsilon}_{k,l}^* e^{ik \cdot x} \Psi_{p,r}(x). \quad (\text{A15})$$

Here we use the Dirac slash notation, $\vec{r}_\perp = \vec{k}_\perp/(sm) - \vec{p}_\perp/m$, where γ^μ are the Dirac gamma matrices. The momentum p'_μ is the momentum of the outgoing electron.

Performing all of the trivial integrations to express the scattering amplitude in the form equation (A4), the invariant amplitude is found to be,

$$\mathcal{M} = -ie \int d\varphi \mathcal{S}(\varphi) \exp \left[i \int_{-\infty}^{\varphi} dy \frac{k \cdot \pi(y)}{\kappa \cdot (p - k)} \right], \quad (\text{A16})$$

where the spin dependent structure is given by,

$$\mathcal{S}(\varphi) = \bar{u}_{p',r'} \left[1 + \frac{m \not{a}(\varphi) \not{k}}{2\kappa \cdot p'} \right] \not{\epsilon}_{k,l}^* \left[1 + \frac{m \not{k} \not{a}(\varphi)}{2\kappa \cdot p} \right] u_{p,r}. \quad (\text{A17})$$

and the classical action in the exponent is expressed in terms of the kinetic, or local, momentum of the incoming electron,

$$\pi^\mu(\varphi) = p^\mu - ma^\mu(\varphi) + \frac{2mp \cdot a(\varphi) - m^2 a^2(\varphi)}{2\kappa \cdot p} \kappa^\mu. \quad (\text{A18})$$

After applying the slowly varying approximation, as detailed above, to the classical action in the exponent, the invariant amplitude equation (A16) can be expressed as

$$\mathcal{M} = -ie \int d\varphi \mathcal{S}(\varphi) e^{iG(\varphi) - iz(\varphi) \sin[b(\varphi) - \vartheta]}. \quad (\text{A19})$$

The function $G(\varphi)$ has the explicit form,

$$G(\varphi) = \frac{1}{2s\kappa \cdot p(1-s)} \int_{-\infty}^{\varphi} dy \left\{ |\vec{k}_\perp - s\vec{p}_\perp|^2 + s^2 m^2 \left[1 + a_0^2 f^2 \left(\frac{y}{\Phi} \right) \right] \right\}, \quad (\text{A20})$$

where we have defined the lightfront momentum fraction $s = \kappa \cdot k / \kappa \cdot p$. As stated above, this only has dependence on the phase through either linear or slowly varying terms.

The term $z(\varphi)$ is

$$z(\varphi) = \frac{ma_0}{\kappa \cdot p(1-s)} \frac{|f(\varphi/\Phi)|}{|\omega(\varphi)|} \sqrt{|\vec{k}_\perp - s\vec{p}_\perp|^2}, \quad (\text{A21})$$

and so the only dependence on the phase comes through the ratio of the slowly varying pulse envelope and the local frequency. The angle ϑ is defined through the relationship,

$$\vartheta = \arctan \left[\frac{(k - sp) \cdot \varepsilon}{(k - sp) \cdot \beta} \right], \quad (\text{A22})$$

and so can be interpreted as the angle between the components of the four-vector $k_\mu - sp_\mu$ projected onto the directions of background field polarisation.

We skip now to the explicit form of the probability. Expanding into Bessel harmonics according to equation (A10), the probability equation (A12) becomes

$$\begin{aligned} \mathbf{P}^{\text{LMA}} = & - \frac{\alpha m^2}{4\pi^2 (\kappa \cdot p)^2} \iint d\varphi d\varphi' \sum_{n, n' = -\infty}^{\infty} \int \frac{ds}{s(1-s)} \int d^2 \vec{k}_\perp e^{iG(\varphi) - iG(\varphi') - inb(\varphi) + in'b(\varphi') + i(n-n')\vartheta} \\ & \times \left(\left\{ 1 + \frac{a_0^2}{2} \left[1 + \frac{s^2}{2(1-s)} \right] \left[f^2 \left(\frac{\varphi}{\Phi} \right) + f^2 \left(\frac{\varphi'}{\Phi} \right) \right] \right\} J_n(z(\varphi)) J_{n'}(z(\varphi')) \right. \\ & \left. - \frac{a_0^2}{2} \left[1 + \frac{s^2}{2(1-s)} \right] f \left(\frac{\varphi}{\Phi} \right) f \left(\frac{\varphi'}{\Phi} \right) [J_{n+1}(z(\varphi)) J_{n'+1}(z(\varphi')) + J_{n-1}(z(\varphi)) J_{n'-1}(z(\varphi'))] \right). \quad (\text{A23}) \end{aligned}$$

The probability in this form contains two infinite sums over the Bessel harmonics and integrals over the outgoing photon momentum. Note the exponential dependence on the chirp function, $b(\varphi)$, and the angle ϑ . If we consider the definitions equations (A20)–(A22), we notice that the only dependence on the transverse photon momentum is through the combination $\vec{r}_\perp = \vec{k}_\perp / (sm) - \vec{p}_\perp / m$. We can then shift the integration variables in equation (A23), and using equation (A22) express the integration measure in polar coordinates,

$$\int d^2 \vec{k}_\perp \rightarrow s^2 m^2 \int d^2 \vec{r}_\perp = \frac{s^2 m^2}{2} \int_0^{2\pi} d\vartheta \int d|\vec{r}_\perp|^2. \quad (\text{A24})$$

The only dependence of the probability on the angle ϑ is then through the exponential factor $\exp(+i(n-n')\vartheta)$. The integration over the angle ϑ sets $n = n'$. This allows the probability to be well approximated by,

$$\begin{aligned} \mathbf{P} \simeq & - \frac{\alpha m^4}{4\pi (\kappa \cdot p)^2} \iint d\varphi d\varphi' \sum_{n=-\infty}^{\infty} \int ds \frac{s}{(1-s)} \int d|\vec{r}_\perp|^2 e^{+iG(\varphi) - iG(\varphi') - in(b(\varphi) - b(\varphi'))} \\ & \times \left(\left\{ 1 + \frac{a_0^2}{2} \left[1 + \frac{s^2}{2(1-s)} \right] \left[f^2 \left(\frac{\varphi}{\Phi} \right) + f^2 \left(\frac{\varphi'}{\Phi} \right) \right] \right\} J_n(z(\varphi)) J_n(z(\varphi')) \right. \\ & \left. - \frac{a_0^2}{2} \left[1 + \frac{s^2}{2(1-s)} \right] f \left(\frac{\varphi}{\Phi} \right) f \left(\frac{\varphi'}{\Phi} \right) [J_{n+1}(z(\varphi)) J_{n+1}(z(\varphi')) + J_{n-1}(z(\varphi)) J_{n-1}(z(\varphi'))] \right). \quad (\text{A25}) \end{aligned}$$

Following through with the local expansion, using equation (A13) and $\theta \ll 1$, the integral over $d\theta$ can be performed, which gives a δ -function:

$$\begin{aligned} \mathbf{P} \simeq & -\frac{\alpha}{\eta_0} \int d\phi \sum_{n=1}^{\infty} \int ds \int d|\vec{r}_{\perp}|^2 \delta \left[|\vec{r}_{\perp}|^2 + 1 + a_0^2 f^2 \left(\frac{\phi}{\Phi} \right) - \frac{2\eta_0 n \omega(\phi)(1-s)}{s} \right] \\ & \times \left\{ J_n^2(z(\phi)) + \frac{a_0^2}{2} \left[1 + \frac{s^2}{2(1-s)} \right] f^2 \left(\frac{\phi}{\Phi} \right) [2J_n^2(z(\phi)) - J_{n+1}^2(z(\phi)) - J_{n-1}^2(z(\phi))] \right\}, \end{aligned} \quad (\text{A26})$$

where we have defined $\eta_0 = \kappa \cdot p/m^2$. The probability only has support when the argument of the δ -function satisfies:

$$|\vec{r}_{\perp}|^2 + 1 + a_0^2 f^2 \left(\frac{\phi}{\Phi} \right) - \frac{2\eta_0 n \omega(\phi)(1-s)}{s} = 0, \quad (\text{A27})$$

which (upon adapting the notation) is found to be *exactly* the stationary phase condition which is evaluated in [58] (see equation (25) of [58]). In that work, the stationary phase approximation is carried out at the level of the amplitude for nonlinear Compton scattering in the slowly varying envelope approximation. Here we have shown that the exact same kinematic relationship reappears at the probability level after the explicit application of a *local expansion*.

The integral over the remaining perpendicular momentum dependence can be trivially carried out using the δ -function in equation (A26), which gives the relatively concise expression (suppressing explicit dependence on ϕ)

$$\mathbf{P} \simeq -\frac{\alpha}{\eta_0} \int d\phi \sum_{n=1}^{\infty} \int_0^{s_{n,*}(\phi)} ds \left\{ J_n^2(z_n) + \frac{a_{\text{rms}}^2}{2} \left[1 + \frac{s^2}{2(1-s)} \right] [2J_n^2(z_n) - J_{n+1}^2(z_n) - J_{n-1}^2(z_n)] \right\}, \quad (\text{A28})$$

where the argument of the Bessel functions is now

$$z_n(\phi) = \frac{2na_{\text{rms}}}{\sqrt{1+a_{\text{rms}}^2}} \sqrt{\frac{1}{\omega(\phi)} \frac{1}{s_n(\phi)} \frac{s}{1-s} \left[1 - \frac{1}{\omega(\phi)} \frac{1}{s_n(\phi)} \frac{s}{1-s} \right]}, \quad (\text{A29})$$

and we have defined the cycle-averaged potential $a_{\text{rms}} = a_0 f(\phi/\Phi)$ and the upper bound on the integration over s is

$$s_{n,*}(\phi) = \frac{s_n(\phi)\omega(\phi)}{1+s_n(\phi)\omega(\phi)}, \quad s_n(\phi) = \frac{2n\eta_0}{1+a_{\text{rms}}^2}. \quad (\text{A30})$$

Thus, when compared with the expressions found for the LMA in a non-chirped pulse [37], the chirp function, $b(\phi)$, contributes an effective *rescaling* of the lightfront energy parameter, $\eta_0 \rightarrow \eta_0 \omega(\phi)$, inside the argument of the Bessel functions. In equation (10) we have redefined s_n and $s_{n,*}$ by absorbing the local frequency, ω (where $\omega = \omega(\phi)$), into the definition of the local energy parameter, $\eta = \eta_0 \omega$ (where $\eta = \eta(\phi)$).

ORCID iDs

T G Blackburn  <https://orcid.org/0000-0002-3681-356X>

B. King  <https://orcid.org/0000-0003-4489-8468>

References

- [1] Ritus V I 1985 Quantum effects of the interaction of elementary particles with an intense electromagnetic field *J. Sov. Laser Res.* **6** 497–617
- [2] Di Piazza A, Müller C, Hatsagortsyan K Z and Keitel C H 2012 Extremely high-intensity laser interactions with fundamental quantum systems *Rev. Mod. Phys.* **84** 1177–228
- [3] Nikishov A I and Ritus V I 1964 Quantum processes in the field of a plane electromagnetic wave and in a constant field 1 *Sov. Phys. JETP* **19** 529–41
Nikishov A I and Ritus V I 1964 *Zh. Eksp. Teor. Fiz.* **46** 776
- [4] Bula C *et al* 1996 Observation of nonlinear effects in Compton scattering *Phys. Rev. Lett.* **76** 3116–9
- [5] Burke D L *et al* 1997 Positron production in multiphoton light-by-light scattering *Phys. Rev. Lett.* **79** 1626–9
- [6] Sarri G *et al* 2014 Ultrahigh brilliance multi-MeV γ -ray beams from nonlinear relativistic Thomson scattering *Phys. Rev. Lett.* **113** 224801
- [7] Sakai Y *et al* 2015 Observation of redshifting and harmonic radiation in inverse Compton scattering *Phys. Rev. Spec. Top.* **18** 060702
- [8] Khrennikov K, Wenz J, Buck A, Xu J, Heigoldt M, Veisz L and Karsch S 2015 Tunable all-optical quasimonochromatic Thomson x-ray source in the nonlinear regime *Phys. Rev. Lett.* **114** 195003
- [9] Yan W *et al* 2017 High-order multiphoton Thomson scattering *Nat. Photon.* **11** 514–20
- [10] Cole J M *et al* 2018 Experimental evidence of radiation reaction in the collision of a high-intensity laser pulse with a laser-wakefield accelerated electron beam *Phys. Rev. X* **8** 011020

- [11] Poder K *et al* 2018 Experimental signatures of the quantum nature of radiation reaction in the field of an ultraintense laser *Phys. Rev. X* **8** 031004
- [12] Meuren S 2019 *Probing Strong-Field QED at FACET-II (SLAC E-320)*
- [13] Abramowicz H *et al* 2021 Conceptual design report for the LUXE experiment (arXiv:2102.02032[hep-ex])
- [14] Erber T 1966 High-energy electromagnetic conversion processes in intense magnetic fields *Rev. Mod. Phys.* **38** 626–59
- [15] Ridgers C P, Kirk J G, Ducloux R, Blackburn T G, Brady C S, Bennett K, Arber T D and Bell A R 2014 Modelling gamma-ray photon emission and pair production in high-intensity laser–matter interactions *J. Comput. Phys.* **260** 273–85
- [16] Gonoskov A *et al* 2015 Extended particle-in-cell schemes for physics in ultrastrong laser fields: review and developments *Phys. Rev. E* **92** 023305
- [17] Lobet M, d’Humières E, Grech M, Ruyer C, Davoine X and Gremillet L 2016 Modeling of radiative and quantum electrodynamics effects in PIC simulations of ultra-relativistic laser–plasma interaction *J. Phys. Conf. Ser.* **688** 012058
- [18] Elkina N V, Fedotov A M, Kostyukov I Y, Legkov M V, Narozhny N B, Nerush E N and Ruhl H 2011 QED cascades induced by circularly polarized laser fields *Phys. Rev. Spec. Top.-Accel. Beams* **14** 054401
- [19] Ridgers C P, Brady C S, Ducloux R, Kirk J G, Bennett K, Arber T D, Robinson A P L and Bell A R 2012 Dense electron–positron plasmas and ultraintense γ rays from laser-irradiated solids *Phys. Rev. Lett.* **108** 165006
- [20] Gelfer E G, Mironov A A, Fedotov A M, Bashmakov V F, Nerush E N, Kostyukov I Y and Narozhny N B 2015 Optimized multibeam configuration for observation of QED cascades *Phys. Rev. A* **92** 022113
- [21] Jirka M, Klimo O, Bulanov S V, Esirkepov T Z, Gelfer E, Bulanov S S, Weber S and Korn G 2016 Electron dynamics and γ and e^-e^+ production by colliding laser pulses *Phys. Rev. E* **93** 023207
- [22] Stark D J, Tonician T and Arefiev A V 2016 Enhanced multi-MeV photon emission by a laser-driven electron beam in a self-generated magnetic field *Phys. Rev. Lett.* **116** 185003
- [23] Grismayer T, Vranic M, Martins J L, Fonseca R A and Silva L O 2017 Seeded QED cascades in counterpropagating laser pulses *Phys. Rev. E* **95** 023210
- [24] Zhang P, Bulanov S S, Seipt D, Arefiev A V and Thomas A G R 2020 Relativistic plasma physics in supercritical fields *Phys. Plasmas* **27** 050601
- [25] Papadopoulos D N *et al* 2016 The Apollon 10 PW laser: experimental and theoretical investigation of the temporal characteristics *High Power Laser Sci. Eng.* **4** e34
- [26] Weber S *et al* 2017 P3: an installation for high-energy density plasma physics and ultra-high intensity laser-matter interaction at ELI-Beamlines *Matter Radiat. Extremes* **2** 149–76
- [27] Gales S *et al* 2018 The extreme light infrastructure-nuclear physics (ELI-NP) facility: new horizons in physics with 10 PW ultra-intense lasers and 20 MeV brilliant gamma beams *Rep. Prog. Phys.* **81** 094301
- [28] Danson C N *et al* 2019 Petawatt and exawatt lasers worldwide *High Power Laser Sci. Eng.* **7** e54
- [29] Harvey C N, Ilderton A and King B 2015 Testing numerical implementations of strong-field electrodynamics *Phys. Rev. A* **91** 013822
- [30] Blackburn T G, Seipt D, Bulanov S S and Marklund M 2018 Benchmarking semiclassical approaches to strong-field QED: nonlinear Compton scattering in intense laser pulses *Phys. Plasmas* **25** 083108
- [31] Di Piazza A, Tamburini M, Meuren S and Keitel C H 2018 Implementing nonlinear Compton scattering beyond the local-constant-field approximation *Phys. Rev. A* **98** 012134
- [32] Ilderton A, King B and Seipt D 2019 Extended locally constant field approximation for nonlinear Compton scattering *Phys. Rev. A* **99** 042121
- [33] King B 2020 Uniform locally constant field approximation for photon-seeded pair production *Phys. Rev. A* **101** 042508
- [34] Chen P, Horton-Smith G, Ohgaki T, Weidemann A W and Yokoya K 1995 Cain: conglomerat d’abel et d’interactions non-linéaires *Nucl. Instrum. Methods Phys. Res. A* **355** 107–10
- [35] Bamber C *et al* 1999 Studies of nonlinear QED in collisions of 46.6 GeV electrons with intense laser pulses *Phys. Rev. D* **60** 092004
- [36] Hartin A 2018 Strong field QED in lepton colliders and electron/laser interactions *Int. J. Mod. Phys. A* **33** 1830011
- [37] Heinzl T, King B and MacLeod A J 2020 Locally monochromatic approximation to QED in intense laser fields *Phys. Rev. A* **102** 063110
- [38] Narozhnyi N B and Fofanov M S 1996 Photon emission by an electron in a collision with a short focused laser pulse *J. Exp. Theor. Phys.* **83** 14–23
- Narozhnyi N B and Fofanov M S 1996 *Zh. Eksp. Teor. Fiz.* **110** 26
- [39] McDonald K 1997 <https://www.physics.princeton.edu/~mcdonald/examples/gaussian2.pdf> (22 March 2021)
- [40] Seipt D and Kämpfer B 2011 Nonlinear Compton scattering of ultrashort intense laser pulses *Phys. Rev. A* **83** 022101
- [41] Seipt D, Kharin V, Rykovanov S, Surzhykov A and Fritzsche S 2016 Analytical results for nonlinear Compton scattering in short intense laser pulses *J. Plasma Phys.* **82** 655820203
- [42] Di Piazza A, Tamburini M, Meuren S and Keitel C H 2019 Improved local-constant-field approximation for strong-field QED codes *Phys. Rev. A* **99** 022125
- [43] Heinzl T and Ilderton A 2017 Exact classical and quantum dynamics in background electromagnetic fields *Phys. Rev. Lett.* **118** 113202
- [44] Heinzl T and Ilderton A 2017 Superintegrable relativistic systems in spacetime-dependent background fields *J. Phys. A* **50** 345204
- [45] Di Piazza A 2014 Ultrarelativistic electron states in a general background electromagnetic field *Phys. Rev. Lett.* **113** 040402
- [46] Di Piazza A 2016 Nonlinear Breit–Wheeler pair production in a tightly focused laser beam *Phys. Rev. Lett.* **117** 213201
- [47] Di Piazza A 2017 First-order strong-field QED processes in a tightly focused laser beam *Phys. Rev. A* **95** 032121
- [48] Boca M and Florescu V 2009 Nonlinear Compton scattering with a laser pulse *Phys. Rev. A* **80** 053403
- [49] Heinzl T, Seipt D and Kämpfer B 2010 Beam-shape effects in nonlinear Compton and Thomson scattering *Phys. Rev. A* **81** 022125
- [50] Mackenroth F and Di Piazza A 2011 Nonlinear Compton scattering in ultrashort laser pulses *Phys. Rev. A* **83** 032106
- [51] Krajewska K and Kamiński J Z 2012 Compton process in intense short laser pulses *Phys. Rev. A* **85** 062102
- [52] Krajewska K, Twardy M and Kamiński J Z 2014 Supercontinuum and ultrashort-pulse generation from nonlinear Thomson and Compton scattering *Phys. Rev. A* **89** 032125
- [53] Heinzl T and Ilderton A 2009 A Lorentz and gauge invariant measure of laser intensity *Opt. Commun.* **282** 1879–83
- [54] Schwartz M D 2014 *Quantum Field Theory and the Standard Model* (Cambridge: Cambridge University Press)
- [55] Wolkow D M 1935 Über eine Klasse von Lösungen der Diracschen Gleichung *Z. Phys.* **94** 250–60
- [56] Baier V N, Mil’shtein A I and Strakhovenko V M 1976 Interaction between a photon and an intense electromagnetic wave *Sov. Phys. JETP* **42** 961–5

- [57] Brodsky S J, Pauli H-C and Pinsky S S 1998 Quantum chromodynamics and other field theories on the light cone *Phys. Rep.* **301** 299–486
- [58] Seipt D, Rykovanov S G, Surzhykov A and Fritzsche S 2015 Narrowband inverse Compton scattering x-ray sources at high laser intensities *Phys. Rev. A* **91** 033402
- [59] Rimbault C, Bambade P, Dadoun O, Le Meur G, Touze F, del C Alabau M and Schulte D 2007 Guinea-PIG++: an upgraded version of the linear collider beam–beam interaction simulation code Guinea-PIG 2007 *IEEE Particle Accelerator Conf. (PAC)* pp 2728–30
- [60] Blackburn T G 2020 Radiation reaction in electron–beam interactions with high-intensity lasers *Rev. Mod. Plasma Phys.* **4** 5
- [61] Baier V N, Katkov V M and Strakhovenko V M 1998 *Electromagnetic Processes at High Energies in Oriented Single Crystals* (Singapore: World Scientific)
- [62] Blackburn T G, Seipt D, Bulanov S S and Marklund M 2020 Radiation beaming in the quantum regime *Phys. Rev. A* **101** 012505
- [63] Harvey C, Heinzl T and Ilderton A 2009 Signatures of high-intensity Compton scattering *Phys. Rev. A* **79** 063407
- [64] Quesnel B and Mora P 1998 Theory and simulation of the interaction of ultraintense laser pulses with electrons in vacuum *Phys. Rev. E* **58** 3719–32
- [65] Seipt D, Heinzl T, Marklund M and Bulanov S S 2017 Depletion of intense fields *Phys. Rev. Lett.* **118** 154803
- [66] Olver F W J 1997 *Asymptotics and Special Functions* (Natick: AKP Classics)
- [67] Dinu V, Harvey C, Ilderton A, Marklund M and Torgrimsson G 2016 Quantum radiation reaction: from interference to incoherence *Phys. Rev. Lett.* **116** 044801
- [68] King B and Ruhl H 2013 Trident pair production in a constant crossed field *Phys. Rev. D* **88** 013005
- [69] Dinu V and Torgrimsson G 2018 Trident pair production in plane waves: coherence, exchange, and spacetime inhomogeneity *Phys. Rev. D* **97** 036021
- [70] Mackenroth F and Di Piazza A 2018 Nonlinear trident pair production in an arbitrary plane wave: a focus on the properties of the transition amplitude *Phys. Rev. D* **98** 116002
- [71] Torgrimsson G 2021 Loops and polarization in strong-field QED *New J. Phys.* **23** 065001
- [72] Di Piazza A, Hatsagortsyan K Z and Keitel C H 2010 Quantum radiation reaction effects in multiphoton Compton scattering *Phys. Rev. Lett.* **105** 220403
- [73] King B 2021 Interference effects in nonlinear Compton scattering due to pulse envelope *Phys. Rev. D* **103** 036018
- [74] De Silvestri S, Laporta P and Svelto O 1984 The role of cavity dispersion in CW mode-locked dye lasers *IEEE J. Quantum Electron.* **20** 533–9
- [75] Ghebregziabher I, Shadwick B A and Umstadter D 2013 Spectral bandwidth reduction of Thomson scattered light by pulse chirping *Phys. Rev. Spec. Top.-Accel. Beams* **16** 030705
- [76] Terzić B, Deitrick K, Hofler A S and Krafft G A 2014 Narrow-band emission in Thomson sources operating in the high-field regime *Phys. Rev. Lett.* **112** 074801
- [77] Rykovanov S G, Geddes C G R, Schroeder C B, Esarey E and Leemans W P 2016 Controlling the spectral shape of nonlinear Thomson scattering with proper laser chirping *Phys. Rev. Accel. Beams* **19** 030701
- [78] Seipt D, Kharin V Y and Rykovanov S G 2019 Optimizing laser pulses for narrow-band inverse Compton sources in the high-intensity regime *Phys. Rev. Lett.* **122** 204802
- [79] Tang S 2021 Generation of quasi-monoenergetic positron beams in chirped laser fields (arXiv:2102.01871[hep-ph])
- [80] Porras M A 1998 Ultrashort pulsed Gaussian light beams *Phys. Rev. E* **58** 1086–93
- [81] Salamin Y I 2007 Fields of a Gaussian beam beyond the paraxial approximation *Appl. Phys. B* **86** 319–26
- [82] Mackenroth F, Holkundkar A R and Schlenvoigt H-P 2019 Ultra-intense laser pulse characterization using ponderomotive electron scattering *New J. Phys.* **21** 123028
- [83] Bagrov V G and Gitman D M 1990 *Exact Solutions of Relativistic Wave Equations* (Netherlands: Springer)
- [84] Heinzl T, Ilderton A and King B 2016 Classical and quantum particle dynamics in univariate background fields *Phys. Rev. D* **94** 065039
- [85] Mora P and Antonsen T M 1997 Kinetic modeling of intense, short laser pulses propagating in tenuous plasmas *Phys. Plasmas* **4** 217–29
- [86] Cowan B M, Bruhwiler D L, Cormier-Michel E, Esarey E, Geddes C G R, Messmer P and Paul K M 2011 Characteristics of an envelope model for laser–plasma accelerator simulation *J. Comput. Phys.* **230** 61–86
- [87] Benedetti C, Schroeder C B, Geddes C G R, Esarey E and Leemans W P 2017 An accurate and efficient laser-envelope solver for the modeling of laser–plasma accelerators *Plasma Phys. Control. Fusion* **60** 014002
- [88] King B, Elkina N and Ruhl H 2013 Photon polarization in electron-seeded pair-creation cascades *Phys. Rev. A* **87** 042117
- [89] Del Sorbo D, Seipt D, Blackburn T G, Thomas A G R, Murphy C D, Kirk J G and Ridgers C P 2017 Spin polarization of electrons by ultraintense lasers *Phys. Rev. A* **96** 043407
- [90] Wistisen T N and Di Piazza A 2019 Numerical approach to the semiclassical method of radiation emission for arbitrary electron spin and photon polarization *Phys. Rev. D* **100** 116001
- [91] King B and Tang S 2020 Nonlinear Compton scattering of polarized photons in plane-wave backgrounds *Phys. Rev. A* **102** 022809
- [92] Seipt D, Ridgers C P, Del Sorbo D and Thomas A G R 2020 Polarized QED cascades (arXiv:2010.04078[hep-ph])
- [93] Blackburn T G 2021 Ptarmigan <https://github.com/tgblackburn/ptarmigan?>
- [94] Blackburn T G 2021 Data for from local to nonlocal: higher fidelity simulations of photon emission in intense laser pulses <https://doi.org/10.5281/zenodo.4632234>